Growth of Colloidal Nanocrystals by Liquid-Like Coalescence**

Growth of Colloidal Nanocrystals by Liquid-Like Coalescence

Bin Yuan[1,2†], Ludovico Cademartiri[1,2,3,4*]

1 Department of Materials Science & Engineering, Iowa State University of Science and Technology, 2220 Hoover Hall, Ames, IA, 50011, USA

2 Department of Chemical & Biological Engineering, Iowa State University of Science and Technology, Sweeney Hall, Ames, IA, 50011, USA

3 Ames Laboratory, U.S. Department of Energy, Ames, IA, 50011, USA

4 Department of Chemistry, Life Sciences, and Environmental Sustainability, University of Parma, Parco Area delle Scienze, 17/A, 43124 Parma, Italy

† Current Address: Mechanical Engineering Department, Carnegie Mellon University, 5000 Forbes Avenue, Pittsburgh, PA, 15213, USA

KEYWORDS (Word Style "BG_Keywords"). If you are submitting your paper to a journal that requires keywords, provide significant keywords to aid the reader in literature retrieval.

ABSTRACT: We here describe, model, and predict the growth kinetics of amine-capped PbS colloidal nanoparticles in the absence of supersaturation. Contrary to expectations, we demonstrate that the particles grow by coalescence (i.e., aggregation followed by reconstruction into a spherical single crystal) rather than by Ostwald ripening, and form distinct subpopulations whose volumes are multiples of the monomer's volume. A comparison of different models indicates that the effective activation energy of coalescence (67.65 $kJ \cdot mol^{-1}$) is composed of two terms of similar magnitude: a term proportional to the contact area between the ligand shells of two colliding particles, and a constant term. Our Brownian dynamics simulations show how the remarkably large rate constants we observed (10^{-2} to 10^{1} $M^{-1} \cdot s^{-1}$) – comparable to those of many bimolecular reactions – are most likely a side effect of the large difference in size between the particles and their mean free path of diffusion. They also show how the low polydispersity observed in the experiments is the likely result of the suppression of collision rates between rare populations due to crowding. The model successfully predicts the growth kinetics of nanoparticles (both particle volume vs time and concentration vs time) synthesized with a series of n-alkylamines of different lengths, therefore enabling the precise control of the average particle size without the need of supersaturation.

Introduction

This paper describes an experimental and computational study of the growth kinetics of oleylamine-capped PbS nanocrystals in the absence of supersaturation. Our claims are:

- Ostwald ripening is not the dominant mechanism of growth in our system. Instead, after the initial burst of nucleation and the consumption of the limiting reagent, growth occurs mainly by coalescence (i.e., penetration of the ligand shell followed by reconstruction into a spherical single crystal), starting from an initial population of monomers. On the other hand, we cannot exclude whether coalescence requires the crystallographic orientation of the particles (i.e., oriented attachment).
- The growth kinetic is quantitatively described by a reaction-limited collisional model that accounts for the influence of ligand length and particle size on the effective activation energy of coalescence.
- The model quantitatively predicts the growth kinetic of PbS nanocrystals grown in the presence of n-alkylamine ligands of different lengths.
- The average value of the activation energy for coalescence that we obtain from the model (67.65 $kJ \cdot mol^{-1}$ where mol refers to moles of nanocrystals, consistently with prior estimates in other materials[1-6]) is likely only an "effective" value that can be explained by an underestimation of collision frequencies by Smoluchowski's equation in crowded colloidal suspensions[7].
- The low polydispersity of the products (~8%) can be explained by the effect of crowding on the rates of collisions.

Furthermore, our analysis led us to the following methodological conclusions:

- The equation widely used in colloidal nanocrystal synthesis to diagnose Ostwald ripening ($D=D_0+k \cdot t^{1/n}$) is not diagnostic. This is a matter of fact. We show that this equation quantitatively describes growth in highly supersaturated,

size-focusing regimes[8] as well as in aggregation-driven regimes. Therefore, Ostwald ripening should not be invoked just on the basis of particle growth rates: other known mechanisms should be first disproven[9]. Our results further suggests that Ostwald ripening could be significantly "overdiagnosed" in the literature[10], since the data required to disprove competing processes (e.g. reaction yield and concentration of particles vs time and temperature) are exceedingly rare in the literature, mostly due to how technically challenging they are to obtain.

- The observation by microscopy of spherical single-crystalline particles does not disprove aggregation-driven growth. Aggregation does not necessarily lead to non-spherical particles. Coalescence can and does happen in nanoscale solids, as prior *in situ* evidence suggested[11].
- Aggregation of nanocrystals does not necessarily lead to large polydispersities of size because, differently from polymers[12], its activation energy depends on size.
- Transmission electron microscopy (TEM) is not necessarily reliable in determining whether coalescence (as opposed to aggregation without reconstruction) is a dominant process of growth. The differences in diameters between the different populations can be smaller than the instrumental resolution (<~2Å) when the size of the monomers is small (e.g. 1 nm) and lower magnifications need to be used to obtain statistically significant sample sizes.
- The effective average activation energy ($1.12 \cdot 10^{-19}$ J) of coalescence between two particles is smaller than the dissociation energy of a single Pb-S bond ($5.74 \cdot 10^{-19}$ J)[13]. Therefore coalescence between nanocrystals can proceed at rates (10^{-2} to 10^{1} $M^{-1} \cdot s^{-1}$) similar to those of bimolecular reactions, for equal concentrations.

While it has been common to believe that colloidal nanocrystal synthesis would allow us to understand the growth of ensembles of crystals (e.g., nanocrystal synthesis[14], additive manufacturing of metals[15]), and while very significant findings have been reported over the years[8,11,16-28], our understanding of it is still in its infancy when compared to the growth of single crystals[29-34].

Summarily, the nucleation and growth of nanocrystals in solution is usually described within the framework developed by LaMer & Dinegar[35], and elaborated by Peng[8] and many others[36,37]. In this framework, a sudden increase in supersaturation[14,38] (obtained through injection[39], decomposition of precursors[40], or a drop in temperature[41]) is used to cause a sudden burst of nucleation. The high supersaturation causes a rapid reduction of the critical size (i.e., the smallest size of a crystal whose growth is favored over its dissolution), thereby facilitating the formation of stable nuclei through fluctuations. Nucleation depletes the activity of the reactants and therefore causes a rapid drop in supersaturation $\sigma \equiv \ln\left(\frac{AP}{K_{sp}}\right)$, where AP is the activity product of the reactants and K_{sp} is the solubility product of the product) which effectively halts nucleation[42]. Between the end of the nucleation phase and the complete depletion of supersaturation, growth is kinetically-controlled and narrows the crystal's size distribution (i.e., focusing phase[8]). As the supersaturation σ decreases, the driving force to growth $\Delta\mu = RT\ln(\sigma)$ decreases, and the critical radius increases ($r_{crit} = \frac{2\Omega\gamma}{\Delta\mu}$ where Ω is the volume per molecule and γ is the interfacial free energy). As the critical radius increases, it "catches up" to the particle size distribution: the particles whose radius is smaller than the critical radius dissolve while the others grow at their expense. This process is called Ostwald ripening[43,44] and it is widely invoked to explain growth in late stages of nanocrystal syntheses (i.e., at low supersaturation).

This Gibbsian description of nucleation and growth is often qualitatively adequate, but it fails to predict the outcome of nanocrystal syntheses[45-47]. This failure is attributed to technical issues (e.g., extreme sensitivity of nucleation rates on the value of ΔG), but also to its assumptions: the capillarity approximation[48,49], neglecting aggregative growth processes[2,18], neglecting the effects of crowding on particle dynamics[50,51], neglecting the role of ligands on the interfacial free energy, surface chemistry[52] and particle-particle interactions[53,54].

Even though significant advances have highlighted the importance of aggregation in particle growth[10,11,16,20,55-60], its mechanistic details are still not fully understood. (i) The experimental systems employed to study aggregative growth often show competing growth mechanisms (e.g. classical addition of molecules/atoms, Ostwald ripening, digestive ripening, etc.)[19,60-65]. The kinetic data has to be described then by a combination of aggregation and other mechanisms[2,61,66]. This complexity increases the degrees of freedom of the models, which lowers the confidence of any fit or conclusion drawn from them[11,67]. (ii) The number of populations observed is usually limited to monomers and dimers[5,63,66,68], and higher oligomers[1,4,6,69] or "polymers"[19] are rarely considered. Fitting kinetic data over narrow ranges of growth decreases the confidence in any fit. (iii) Kinetic models were often developed on deficient data: ideally, the temporal evolution of average size, concentration, and polydispersity should all be characterized[11]. However, in nearly every instance, the average size was the only observable to be considered,[5,10,66,70,71] usually due to the technical challenges of measuring particle concentrations. (iv) Many characterizations were conducted at a single temperature (with exceptions[1,3-6,61,63,70]) and could not extract activation energies or test mechanistic hypotheses about the aggregation process[10,60,64,72-75]. Fitting single temperature data decreases the confidence in the model because it does not prove that the model works across temperatures. (v) Many models involve parameters with no clear physical meaning[59], overlooked important variables (e.g., ligands[2,3,5,70,76]), or are only applicable to special cases[77,78] (e.g. the formation of dimers[5,63,66,68], aggregation between specific populations[3,10], formation of anisotropic nanocrystals[19,68]). For example, the use of capping ligands in the synthesis of nanocrystals in organic solvents is extremely common[14]. It is well known that the length of the ligands influences the aggregation process[6,11,20,79-85]. However, its effect has not been modeled[1,3,4,66,69,86] probably because most systems employed for kinetic studies were grown in aqueous conditions[63]. Moreover, while aggregation can depend on the size of the particles[1,11,74,87] due to its influence on their mutual interactions (i.e., affecting collision rates), the size-dependence of the activation energy was generally not considered when models were developed to fit the experimental data[1]. (vi) Lastly, and most importantly, models

were derived by fitting experimental data and their ability to predict particle growth kinetics is unproven[72,74].

Therefore, we developed a model system that overcomes most of the technical challenges associated with the kinetic study of crystal growth in the absence of supersaturation. We were then able to model, simulate and predict experimentally obtained growth kinetics.

Experiment Design

We chose as a model system the reaction between oleylammonium hydrosulfide (OLAHS) and $PbCl_2$ in oleylamine to form PbS nanocrystals[88]. We conducted reactions by injecting OLAHS into the $PbCl_2$/oleylamine slurries at five different temperatures (80, 100, 120, 140, and 160 °C), and characterized the products at sixteen reaction times (1, 2, 4, 6, 8, 10, 12, 14, 16, 20, 24, 30, 36, 42, 50, and 60 minutes).

As a control experiment, we synthesized PbS nanocrystals in conditions of supersaturation-driven growth ("addition" conditions). Briefly, this hot-injection reaction was conducted at 100 °C by the injection of a solution of S_8 (1.480 mM) in oleylamine into a $PbCl_2$ slurry in oleylamine (1.417 mM). These heterogeneous reaction conditions have been shown to yield highly uniform particles through a protracted focusing (i.e., high supersaturation) phase that is caused by the gradual dissolution of the $PbCl_2$ precursor and slow reactivity of the S_8-oleylamine solution[89,90]. While the sulfur precursor is different (S_8 vs OLAHS), current understanding indicates that the active species in both precursors is H_2S[88,91], thereby making the two reactions chemically analogous.

This model system was fulfilled the numerous requirements (listed below) associated with a complete quantitative analysis of the growth kinetic of colloidal nanocrystals in the absence of supersaturation.

Easily quantifiable concentration and size of the nanocrystals. An accurate characterization of the aggregative growth kinetics of nanocrystals requires the characterization of the concentration and the size distribution of the nanocrystals. Ideally it should be able to distinguish individual populations of nanocrystals formed from the aggregation of an initial monomer population (i.e., distinguishing monomers from dimers, trimers from tetramers, etc…) and associate a concentration to each population.

The characterization of particle size distributions with very high resolution (~1Å) is challenging. Analyses of powder X-ray diffraction (XRD) either by Scherrer or Rietveld methods can require significant amount of material, require assumptions on the shape of the nanocrystals, and provide only values of the average size[92]. Transmission Electron Microscopy (TEM) characterizations can instead provide size distributions, but are extremely time- and resource-intensive and (as we show in this work) do not provide the combination of resolution and statistical power that is required to exclude certain growth mechanisms.

Concentrations of nanocrystals in their colloidal state are notoriously difficult to measure. Thermal Gravimetry Analysis (TGA) is susceptible to significant (>20%) errors due to incomplete removal of the organic fraction[93]. Inductively-coupled plasma atomic emission spectroscopy (ICP-AES) can be sufficiently quantitative, but requires highly purified colloids and is technically demanding[94,95].

PbS nanocrystals provide a solution to these challenges. Due to their large exciton Bohr radius, their excitons are strongly confined[96]. As a result, the energies of the excitonic transitions vary strongly with the size of the particles. This dependency has been carefully measured and validated in independent experiments[95,97]. The excitonic transition with lowest energy (1S1S) is significantly separated in energy from the next transition, therefore yielding an absorption peak with minimal overlap (as opposed to Cd chalcogenides[98]). Furthermore, PbS nanocrystals are one of the few nanoparticles whose extinction coefficient (and its dependence on size) is known with reasonable accuracy (~20% uncertainty)[95] and quantitatively validated experimentally[97] and theoretically[99] by separate groups. In summary, the 1S1S absorption peak of a dispersion of PbS nanocrystals allows for the simultaneous determination of the average size of the particles and their concentration.

Representative of a broader class of materials. A model system should be ideally representative of a much broader class of materials. PbS is representative of IV-VI semiconductors and, to an extent, of sulfides in general.

Negligible Ostwald ripening. A significant influence of Ostwald ripening would compromise the ability to isolate the contribution of aggregative processes on the growth kinetics. Our prior work has shown that, when synthesized from $PbCl_2$, PbS nanocrystals did not show evidence of ripening in the late stages of reaction[89]. These observations have been recently validated even when lead oleate was used as a metal precursor[100].

Negligible supersaturation. To eliminate the contribution of classical growth (i.e., addition of molecular/ionic species to the nanocrystal surface) it is essential for supersaturation to be as low as possible immediately after the nucleation phase. We recently developed an ionic liquid sulfur precursor (oleylammonium hydrosulfide, OLAHS) obtained from the reaction of H_2S and oleylamine that reacts to completion immediately after its injection[88]. The reaction yield was shown to be constant after nucleation and no free sulfur precursor was detected.

Highly concentrated reactions. Aggregative processes follow, in first approximation, a second order kinetic[59,101,102] where the rate is proportional to the product of the concentrations of the colliders. Therefore, syntheses that produce the highest possible concentrations of nanocrystals are desirable to maximize the influence of aggregation[88,103,104]. As we showed in a prior work, the synthesis of PbS nanocrystals with OLAHS allows to obtain the highest concentrations ever reported in nanoparticle synthesis[88].

Isotropic aggregative growth. The quantification of growth rates from absorbance spectra is only reliable if the shape of the nanocrystals is conserved since the energies of the exciton transitions depend on particle shape[105]. During the development of our model system we hoped that aggregation of our PbS nanocrystals would be accompanied by reconstruction (i.e., coalescence), as shown in prior work in liquid-cell TEM.

Results and Discussion

Growth in conditions of high supersaturation (control experiment)

Before discussing the growth of the nanocrystals in the absence of supersaturation, we show how the same nanocrystals grow when supersaturation is abundant (i.e., our control experiment). Figure 1a shows the evolution of optical absorption spectrum of PbS nanocrystals grown in our control experiment. The peak at highest wavelength is due to the 1S1S exciton transition[106]. Other features above the background correspond to higher energy transitions[95].

The number-averaged particle concentration and the average size of the particles were obtained for each sample by the following process. First, the average size of the particles in the dispersion was calculated by taking the energy of the 1S1S exciton (E1) transition and solving the following empirical equation[95] for the core radius r: $E_1[\text{eV}] = 0.41 + 0.96 \cdot r^{-2} + 0.85 \cdot r^{-1}$.

The average size of the nanocrystals was then used to calculate the extinction coefficient by using the empirical equation[95] $\varepsilon[\text{M}^{-1}\cdot\text{cm}^{-1}] = 2030790 \cdot r^{2.49}$.

Lastly the concentration was obtained from Lambert-Beer's equation $A = \varepsilon \cdot c \cdot l$ where c is the concentration of nanoparticles (in M units), l is optical path length (in cm units) and A is the integrated absorbance of the 1S1S exciton peak (approximated as twice the integral of the low-energy half of the peak).

The concentration of the particles (in particles·m^{-3}) as a function of time (in seconds) is shown in Figure 1b. The concentration of particles does not change significantly and remains at ~$0.15 \cdot 10^{23}$ particles·m^{-3} (~$2.5 \cdot 10^{-2}$ mM). On the other hand the number-averaged volumes of the particles (shown in Figure 1c in units of nm^3) increase with time as a power law that extrapolates to an initial volume of 44 nm^3 (diameter = 4.4 nm). Importantly, even though we are clearly not in Ostwald ripening regime, the Ostwald ripening equation $D - D_0 = k(t - t_0)^{\frac{1}{n}}$ (where D is diameter, k is the rate constant, t is the reaction time, n is the growth exponent, and subscript 0 identifies the values of D and t at the beginning of the reaction) fits very well these data (R^2=0.996) with a value of n (1.9±0.1) which is acceptable for Ostwald ripening[5] (between 2 and 4, depending on the rate-limiting transport process[66]).

The yield (shown in Figure 1d in percentage units) shows a steady increase from ~15% to ~60% between 1 min and 1 hr. Lastly, the size polydispersity of the nanocrystals as a function of time was estimated by converting the 1S1S absorption peak (after removal of the background absorption) into a size distribution and then obtaining the mean and standard deviation. This estimate is bound to overestimate polydispersity as it implicitly interprets the intrinsic line-width of the transition as being caused by polydispersity. The data (cf. Figure 1d) shows that the polydispersity remains constant throughout the reaction at a low value of ~4.5%.

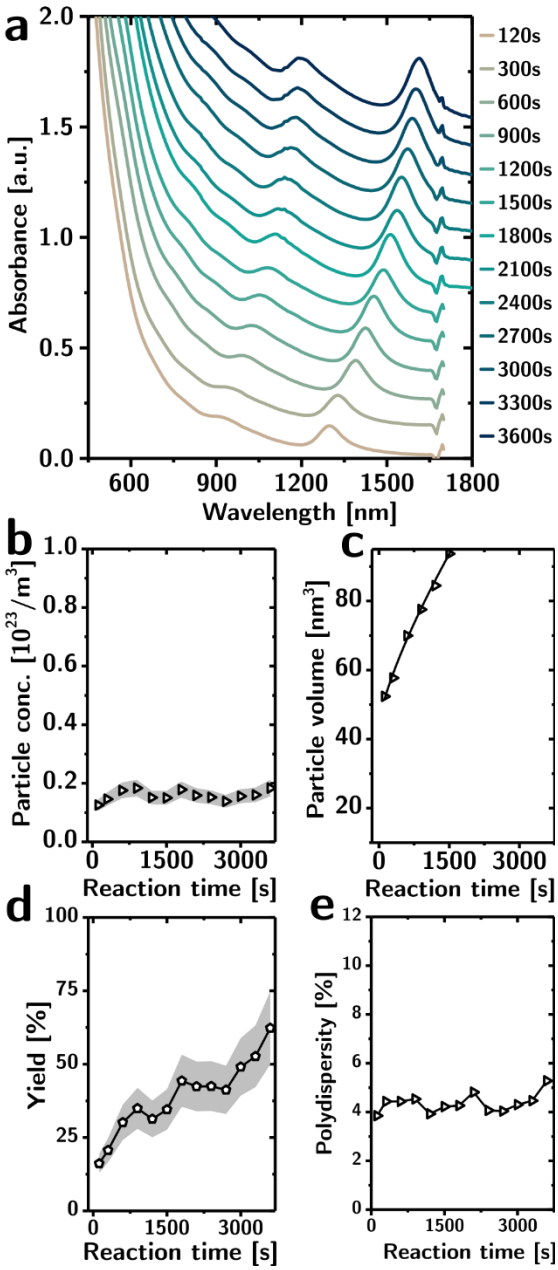

Figure 1. Growth kinetics of PbS nanocrystals in the presence of supersaturation. (a) Absorption spectra (offset for clarity), (b) concentration of particles, (c) number-averaged particle volume, (d) reaction yield, and (e) polydispersity as a function of reaction time. In both panel b and d the grey area indicates the uncertainty on the mean value.

In summary, the growth kinetics in the control experiment is consistent with classical supersaturation-driven growth. The number of particles does not change significantly during growth thereby indicating the absence of particle-generating mechanisms (e.g., secondary nucleation) or particle-depleting mechanisms (e.g., Ostwald ripening, aggregation). The steady increases in time of the particle volumes and reaction yield are consistent with a nearly constant supersaturation. Finally, the low polydispersity is consistent with the simultaneous generation of the nuclei at the beginning of the reaction and the absence of coarsening mechanisms (e.g., Ostwald ripening, aggregation, etching).

In the absence of supersaturation growth occurs by coalescence

When the sulfur precursor used is depleted in the nucleation phase, there is no opportunity for the particles to grow by classical addition mechanisms. Oleylammonium hydrosulfide (OLAHS) dissociates rapidly at high temperatures into oleylamine and hydrogen sulfide[88]. After injection in the $PbCl_2$ slurry, the liberated H_2S reacts quickly to form PbS, while unreacted H_2S leaves the system as a gas. The lack of free sulfur precursor creates conditions of minimal supersaturation which exclude classical growth processes. These claims were proven in our prior work[88] and are validated here.

The reaction yield as a function of time and temperature with OLAHS (cf. Figure 2a) is approximately constant throughout the reaction at ~73 ± 15% (mean ± standard deviation) and independent of temperature. The spread in the data is attributed to the uncertainty of the extinction coefficient (±20%)[95].

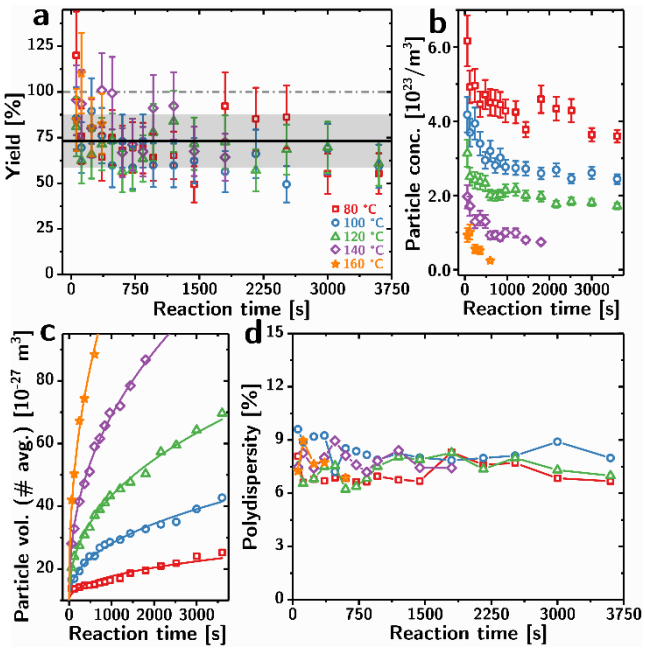

Figure 2. Growth kinetics of PbS nanocrystals in the absence of supersaturation. (a) Reaction yield (black line: mean, grey band: one standard deviation about mean), (b) concentration of particles (data is offset for clarity to show the decrease over time), (c) number-averaged particle volumes (globally fitted with power law), and (d) polydispersity as a function of time (abscissa), and temperature (legend in panel a). Lines are added for clarity.

The concentration of particles as a function of time and temperature is shown in Figure 2b. It starts off at much higher values than in the control experiment (up to ~$3.5 \cdot 10^{23}$ nanocrystals·m^{-3} or ~0.5 mM, consistently with the use of a more reactive precursor), but then decreases rapidly with time. The rate at which the concentration drops increases with temperature. The number-averaged volumes of the particles (in m^3) as a function of time and temperature (cf. Figure 2c) shows a familiar saturation curve with rates increasing with temperatures. Lastly, the polydispersity (cf. Figure 2d) remains remarkably constant throughout the reaction at a relatively low value of 8% regardless of the reaction temperature.

These data, taken together, exclude addition as a growth mechanism. The evolution of yield, concentration, and volumes are instead consistent with both aggregation and Ostwald ripening: the total concentration of particles decreases in time in spite of a constant reaction yield, and their average volume increases. While the exponent obtained by fitting the experimental data in Figure 2c with the Ostwald ripening equation (4.0±0.1) is compatible with our understanding of that process, other experimental data (shown below) is fundamentally inconsistent with Ostwald ripening.

Structural characterization of the products by TEM showed (cf. Figure 3a) that the particles were roughly spherical and monocrystalline. XRD (Figure 3b) confirms that the material was indeed PbS, phase pure and crystalline. The spherical shape of the particles disproves "aggregation without reconstruction" as a dominant mechanism of growth. Nonetheless, coalescence has been observed between inorganic nanocrystals in liquid-cell TEM experiments[11,16,107-109].

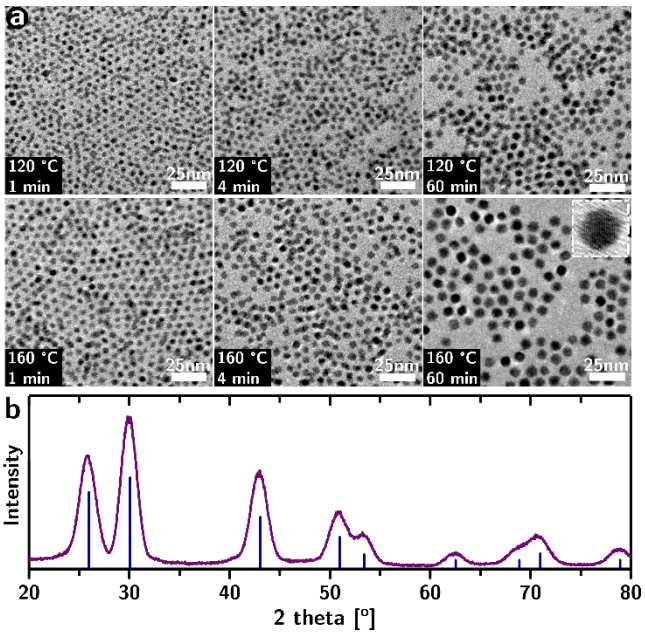

Figure 3. Morphology and structure of the particles after growth in the absence of supersaturation. (a) Representative TEM micrographs of PbS nanocrystals obtained after 1, 4, and 60 min of growth at 120 °C (top row) and 160 °C (bottom row). (b) XRD pattern of the nanocrystals with overlayed peak positions for PbS (galena, PDF#00-005-0592).

Additional crucial information is obtained from the analysis of the optical absorption spectra of the samples. Figure 4a shows the evolution of the 1S1S absorption peak (after background subtraction) as a function of time for a reaction at 100 °C in the absence of supersaturation. By comparison, we show in Figure 4b the same data from the control experiment. While the control experiment shows a gradual shift to lower energies of a single Gaussian peak (a Kolmogorov-Smirnov test[110] conducted on the background-subtracted data did not reject the normal distribution), the same absorption peak in the absence of supersaturation is distinctly non-Gaussian. Its features and

shoulders are present at all reaction temperatures (cf. Figure 4c) and suggest the convolution of multiple sub-peaks, i.e., the presence of multiple populations of particles.

The shift to higher wavelengths of the 1S1S peak in Figure 4a appears to result from the reduction in intensity of sub-peaks at short wavelengths and the increase in intensity of sub-peaks at long wavelengths. To test this hypothesis we deconvoluted the 1S1S peaks into individual, Gaussian sub-peaks. A second derivative analysis of the spectra was used to guide the deconvolution, which yielded, for each spectrum, a minimum set of two to four sub-peaks with R^2>0.99. For each sub-peak we could extract the number-averaged volume and concentration of the population representing it, as discussed above.

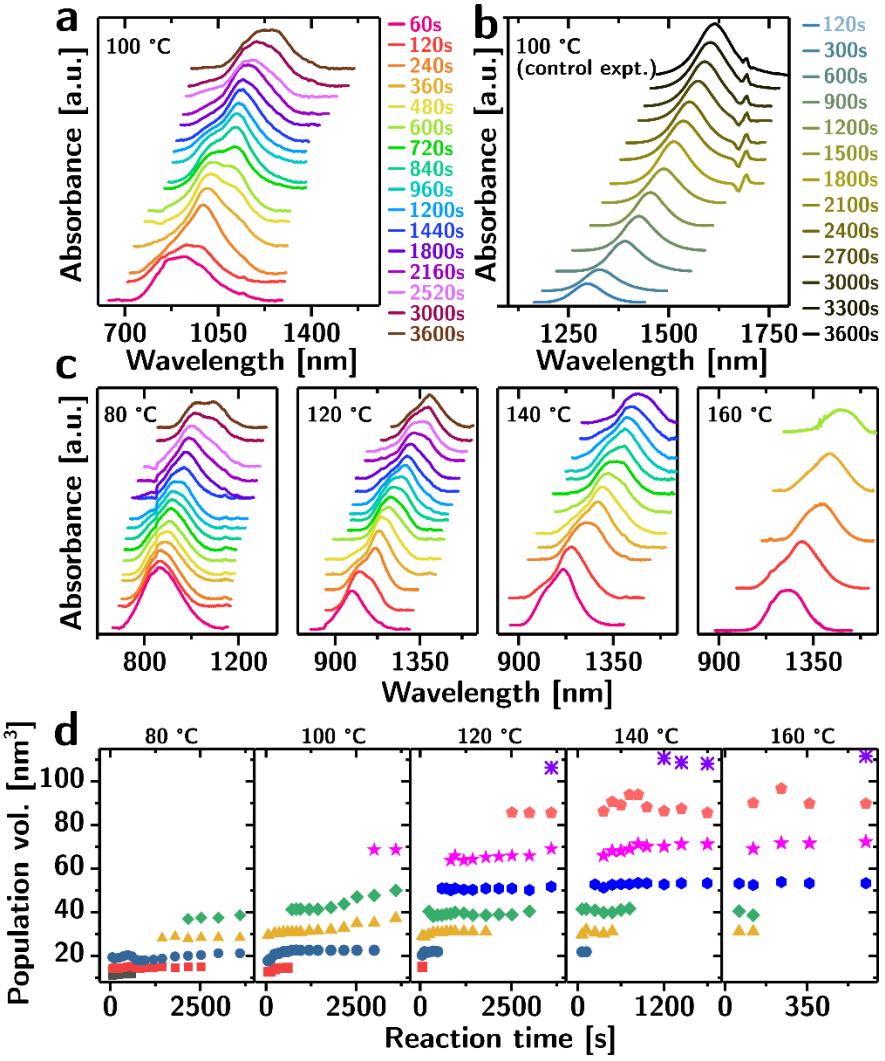

Figure 4. Optical characterization of PbS nanocrystals grown in the absence of supersaturation. (a-b) Comparison of the evolution during growth at 120 °C of the absorption peak from the 1S1S transition (background subtracted) in the absence (a) and (b) presence of supersaturation. (c) As panel (a) but for reactions at 80 °C, 120 °C, 140 °C, 160 °C. (d) Particle volumes of the individual populations as a function of reaction time (absissa) and temperature (80 °C, 100 °C, 120 °C, 140 °C, 160 °C from left to right).

The plot in Figure 4d is composed of 5 panels, one for each reaction temperature, from 80 °C (left) to 160 °C (right). The abscissa indicates the reaction time while the ordinate indicates the number-averaged volumes of the individual populations. The volumes appear to be remarkably concentrated around specific values (color-coded for clarity) which are largely constant in time, and, most strikingly, conserved across reaction temperatures!

If the features from the absorption spectra were the result of noise, the volumes identified in Figure 4d would be randomly distributed. They are not. A kernel density analysis of all observed volumes (bandwidth=2 nm^3) show a multimodal distribution (cf. Figure 5a). If these distinct volumes were caused by a coalescence process, they would be multiples of a specific monomer volume. Therefore, we tested whether we could find a monomer volume that, if used to divide the population volumes shown as peaks in Figure 5a, would result in the minimal fractional volumes. The sum of the fractional volumes as a function of a hypothetical monomer volume (cf. Figure 5b) shows that there is a clear minimum for a value of 9.653 nm^3 (corresponding to a radius of 1.321 nm). The plot in Figure 5c shows the modes from Figure 5a as a function of the ratio be-

tween their volumes and 9.653 nm^3. As shown by the droplines, the modes align qualitatively with integers, i.e., the populations identified by spectroscopy would be the dimers, trimers, tetramers, pentamers, eptamers, ennamers, and undecamers. The small discrepancies can be attributed to (i) slight differences in the size of the monomers obtained at different reaction temperatures, and (ii) the overlapping of peaks in the absorption spectrum[6]. Furthermore, it is important to note that, given that our determination of the populations is indirect and relies on a deconvolution, not all populations might have been detected, and that similarly sized populations do not necessarily have comparable concentrations[6].

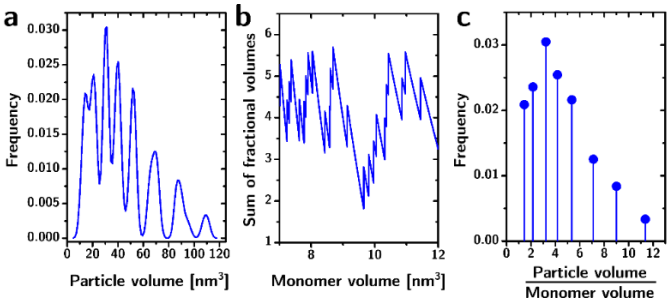

Figure 5. Statistical analysis of the volumes of the populations. (a) Kernel density analysis of the distribution of volumes (combined reaction times and temperatures), showing distinct peaks. (b) Sum of all fractional volumes as a function of the monomer volume, identifying an optimal monomer volumes at ~9.65 nm^3. (c) Peaks from panel a, rescaled as multiples of the optimal volume identified in panel b.

A separate test for the existence of a starting monomer was to extrapolate the datasets of number-averaged particle volumes vs time (cf. Figure 2c) to time = 0. To do so, we used the power law fit that is shown in Figure 2c. Remarkably, the datasets for all temperatures converge to the same starting nanocrystal volume of 9.750 ± 0.71 nm^3 which is within 1% of the value obtained from the analysis of individual population volumes in Figure 5B.

A similar extrapolation conducted on mass-averaged volumes yields a value of 9.87 ± 0.70 nm^3. The ratio between the mass-averaged and number-averaged estimate for the monomer volume (i.e., the polydispersity index, PDI = 1.012 ± 0.15) cannot establish whether the monomer is monodisperse or not.

TEM evidence cannot easily disprove coalescence as a growth mechanism

While the estimation of sizes from optical properties is well established, many colleagues in the scientific community believe that the TEM is the only trustworthy characterization that can prove the multimodality of a size-distribution. So, we did characterize a sample of those shown in Figure 3a by TEM and measured particles diameters (n=326). The size distribution is shown in Figure 6a as a histogram (bin size=0.19 nm) and as a kernel density function (bandwidth=0.19 nm). The bin size and bandwidth were chosen to match the resolution of our TEM: one should not lightly claim features in the size distribution that are smaller than the resolution of the instrument. The resulting distribution, while not Gaussian, does not show any obvious shoulder.

By comparison, the absorbance of the 1S1S transition of the same sample shows a clear shoulder and what is most likely a convolution of two peaks. After conversion to diameter by using Equation 1, the size distribution still shows a pronounced shoulder. If one takes this optically-derived size distribution and bins the data with a resolution of 0.19 nm, one obtains a distribution (Figure 6d, solid line), which is remarkably similar to the TEM results (Figure 6d, dashed line). The difference in the average diameters between the two distributions (3.71 nm from the absorption data vs 3.90 nm from the TEM data) is expected. As we originally wrote in 2006 on the basis of compositional data[89], the surface of the particles is terminated by a layer of $PbCl_2$. This shell is accounted by TEM, but not by the exciton energy ($PbCl_2$ is an insulator). The difference in the radii (0.095 nm) is a third of the shortest Pb-Cl bond (0.283 nm) in the $PbCl_2$ structure, consistent with a (sub)monolayer shell.

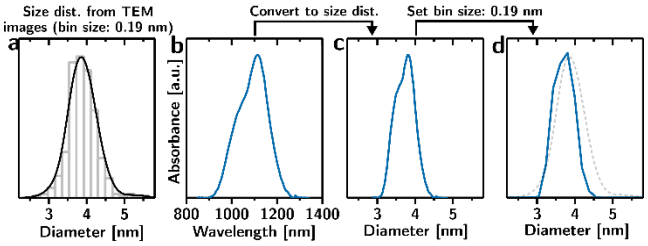

Figure 6. Demonstration of the inadequacy of TEM-derived data in uncovering multimodal size distributions originating from coalescence. (a) Size distribution of PbS colloidal nanocrystals obtained by coalescence (histogram and kernel density with bin size/bandwidth equal to the resolution of the microscope, 0.19 nm). (b) 1S1S absorption peak of the same sample characterized in panel a. (c) Size distribution obtained by converting the absorption data in panel b by using Equation 1. (d) Binning the distribution from panel c with a 0.19 nm bin size, and comparison with the TEM-derived distribution (dashed line).

This analysis demonstrates that a monomodal distribution obtained by a TEM analysis, even with good statistics (e.g., hundreds of particles), cannot prove that the size distribution does not feature subpopulations resulting from coalescence. The instrument resolution, limitations in sample size, the ratios of the concentrations between different populations, and the intrinsic limits of its size characterization (conversion of a diameter/area size information to volumes carries an error), do not allow to distinguish the different modes in the size distribution that could emerge from coalescence of particles starting from a small monomer population. For example, if the monomer has a volume of 10 nm^3 (i.e., diameter = 2.673 nm), the difference in radius between a pentamer and a hexamer would be 0.14 nm, and this without adding the confounding effect of polydispersity. While the physical reason why optical data can provide a higher resolution in the size distribution is that the spectrometer's resolution (~1 nm) translates into a size resolution of ~10^{-12} m (homogeneous linewidth permit-

ting), the statistical reason is that it can sample trillions of particles with each spectrum, instead of hundreds/thousands[111] as in the case of TEM.

In summary, the data in Figures 4 and 5 indicate that growth in the absence of supersaturation proceeds by coalescence, starting from an initial population of ~10 nm^3 monomers. The small value of size polydispersity (~8%) is one apparently contradictory piece of evidence. Nonetheless, aggregation does not (per se) imply a rapidly increasing polydispersity: if the activation energy of the process is dependent on the size of the particle, then the polydispersity can remain narrow.

The experimental results are inconsistent with Ostwald ripening

Ostwald ripening is often invoked to explain particle coarsening in conditions of low supersaturation. Our data is inconsistent with it for the following reasons:

1. Ostwald ripening does not cause by itself bimodal/multimodal volume distributions[10,59]. The data in Figure 4 and 5 show that the dispersion is composed of polydisperse but separate populations of particles.
2. In the presence of distinct size populations, Ostwald ripening would shift the volumes of the individual populations with time. If coalescence and Ostwald ripening coexist, the size of the larger populations would gradually increase over time accompanied by the decrease in the size of the smaller populations due to Ostwald ripening[10]. We do not observe any significant shift, as shown in Figure 4d. The sharp peaks in the kernel density shown in Figure 5a are additional evidence for the lack of coarsening.
3. The polydispersity is low and does not increase over time. Colloids undergoing ripening show polydispersities that are much larger than 8%: Monte Carlo simulations of nanoparticle distributions undergoing Ostwald ripening predicted a steady state polydispersity of 20%[112].
4. The Ostwald ripening equation is not diagnostic. While the particle growth kinetics shown in Figure 2c can be indeed fitted well with the Ostwald ripening equation with a physically plausible exponent *n*, the same equation also fits the growth kinetics of the control experiment, as shown in Figure 1c. The control experiment has sufficient supersaturation to cause a rapid increase in yield, and does not show a decrease in the number of particles, as expected from Ostwald ripening.

Ostwald ripening is usually invoked as the simplest explanation for particle growth in the absence of significant supersaturation. In most reported cases, the kinetic data reported was not sufficient to disprove Ostwald ripening. In such cases, postulating that Ostwald ripening was the dominant growth mechanism was consistent with the principle of parsimony,[113] but was inconsistent with the "burden of disproof"[9].

We show in the following pages how coalescence is equally simple as a model (i.e., it has the same degrees of freedom, two), but is instead fully consistent with the experimental data described here. And therefore provides a better explanation for our observations.

A simple coalescence model quantitatively describes the observed growth kinetics

Modeling population balances

We developed a computational model for the growth kinetic based on population balance equations[55,57,114]. Consider the simplest case of a collection of N_1 spherical monomers of radius r_1 and that these monomers coalesce in a reaction-limited process to form spherical dimers of radius $r_2 = 2^{1/3} r_1$. The process is described by coupled equations describing the creation and annihilation processes:

$$\frac{dN_2}{dt} = \frac{1}{2} k_{11} N_1^2 \qquad \text{Eq. 1}$$

$$-\frac{dN_1}{dt} = k_{11} N_1^2 \qquad \text{Eq. 2}$$

where k_{11} is the rate constant (commonly referred to as the kernel) for the coalescence between monomers defined by the Arrhenius equation

$$k_{11} = Q_{11} e^{-\frac{E_{a,11}}{k_B T}} \qquad \text{Eq. 3}$$

where Q_{11} is a prefactor that quantifies the collisional rate between monomers, $E_{a,11}$ is the activation energy for the coalescence of two monomers, k_B is Boltzmann's constant and T is the reaction temperature.

If we consider a coalescence process that produces a maximum of *p* populations (for computational convenience), then the system is described by a system of *p* differential equations

$$\frac{dN_n}{dt} = \begin{cases} -\sum_{m=2}^{p-1} k_{1,m} N_1 N_m, & n = 1 \\ \sum_{m=1}^{n-1} \frac{1}{2} k_{n-m,m} N_{n-m} N_m - \sum_{m=1}^{p-n} k_{n,m} N_n N_m, & 1 < n < p \\ \sum_{m=1}^{p-1} \frac{1}{2} k_{p-m,m} N_{p-m} N_m, & n = p \end{cases} \qquad \text{Eq. 4}$$

Modeling the activation energies

The kernels $k_{n,m}$ describe the physics of the process and, specifically, the activation energies describe the mechanism of coalescence. We initially considered for the activation energy a general expression of the following type:

$$E_{a,nm} = \frac{C}{\left(\frac{1}{r_n + l_n} + \frac{1}{r_m + l_m}\right)} + D(r_n^E + r_m^E), \qquad \text{Eq. 5}$$

where *C*, *D*, and *E* are fitting parameters that are independent of particle size, time, or temperature, while l_n and l_m are the thicknesses of the ligand shells for the respective *n* and *m* populations.

We expression for the activation energy is meant to quantify two processes (cf. Figure 7a). The first term quantifies the net energy cost of penetrating the ligand shell and is proportional to the contact area between the ligand shells[54]. The second term quantifies the net energy cost of coalescing the particles, after ligand shell penetration has occurred. Given the lack of information on the details of this last mechanism, we opted to describe it agnostically with a power-law dependence on the radius of the particles. There are multiple reasons why the reconstruction process could depend on the size of the particles

involved. For example, oriented attachment is thought to involve an orientation step in which the particles are rotating with respect to each other to find mutual crystallographic orientation[16]. It is conceivable that the rate of this process would scale inversely with the mass of the particles.

Modeling the thickness of the ligand shell as a function of particle size

The dependence of the thickness of a ligand shell as a function of its grafting density, Kuhn length, and contour lengths has been well described for flat surfaces[115]. At high grafting densities and in the strong stretching regime (the common scenario for ligand-capped nanocrystals), the thickness of the shell *l* can be described as

$$l = Z\left(\frac{12b^5\Gamma\omega}{\pi^2}\right)^{1/3} \qquad \text{Eq. 6}$$

Where *Z* is the number of Kuhn segments in the ligand, *b* is the length of the Kuhn segment, *Γ* is the grafting density, and *ω* is the excluded volume parameter. Equation 6 does not consider the curvature of the surface, which can have a significant influence on the conformation of ligands[54]: for equal grafting densities, a convex surface provides the ligands with more accessible volume (and therefore, more entropy) than a flat surface. The volume available for each ligand determines its stretching. Recent reported models for ligand shells on nanocrystals focused on the dry state[116], while our experiments take place in solution, where partial solvation significantly changes the ligand shell thickness[117].

Our approach to account for curvature is to estimate the grafting density on a flat surface that would provide the ligands with the same amount of available volume that they have on surface of the nanocrystal. In brief, we calculated the grafting density on the particles by assuming 33% coverage, i.e., 33% of the exposed lead ions are coordinated by one oleylamine molecule. (Incomplete coverage is common in colloidal nanocrystals[52,118,119] and relatively large differences in *Γ* do not have a large effect on *l* due to the 1/3 exponent in Equation 6). Then we calculated, as a function of particle size, the number of ligands per particle, and the amount of volume available to the bound ligands (i.e., the volume of a shell as thick as the contour length of oleylamine, l_0, divided by the number of ligands). We then calculated how many ligands would be grafted on an equivalent but flat surface if they had the same amount of volume available. On the basis of this number we could calculate the effective grafting density to be used in Equation 6. This procedure yields the following analytical function of the ligand shell thickness as a function of the particle radius

$$l(r) = N\left(\frac{36\omega\Gamma b^5}{\pi^2}\frac{r^2}{3r^2+3rl_0+l_0^2}\right)^{\frac{1}{3}} \qquad \text{Eq. 7}$$

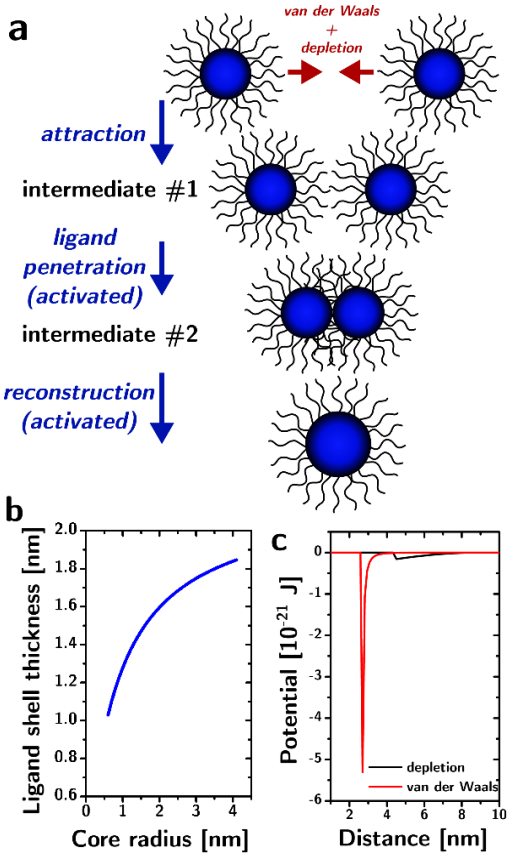

Figure 7. Modeling of the coalescence process. (a) Sketch of the two step process of coalescence involving ligand-shell penetration and reconstruction. (b) Graph of the thickness of the ligand shell as a function of core radius (red circles) and logistical fit. (c) Comparison of van der Waals and depletion potentials as a function of distance at the beginning of the reaction.

For surface-bound oleylamine in oleylamine (our reaction conditions) we used a Kuhn length of 14 Å (i.e., N=1.62) and an excluded volume parameter of 0.2[120] and obtained the data shown in Figure 7b. The data is plausible: as r tends to infinity, the value of *l(r)* approaches l_0.

Modeling the collision frequencies

The first description of collision rates was developed by Smoluchowski for the case of diffusion-limited aggregation in dilute conditions[7]. In spite of its significant limitations[114] (which are discussed later on) we chose to use this model for its simplicity and well understood assumptions. The collision frequencies were corrected to account for the interactions between particles[121], and expressed as

$$Q_{n,m} = \frac{4\pi(R_n+R_m)(D_n^0+D_m^0)}{W} \qquad \text{Eq. 8}$$

where $Q_{n,m}$ is the collision rate between particles of the *n* and *m* populations, *W* is the correction factor that accounts for the effect of interactions, *R=r+l*, and $D^0{}_n$ is the diffusivity of the colloids calculated according to the Stokes-Einstein equation (assuming spherical particle shapes) $D_n^0 = k_B T/6\pi\eta R_n$, where η is the dynamic viscosity, which depends on temperature ac-

cording to a phenomenological equation reported for the similar molecule oleic acid[122] $\eta(T) = 3.18 \cdot 10^{-3} + 1.153 \cdot T^{-11.02}$.

Interactions can significantly modify the collision frequencies. For a given potential between the particles *E(x)*, the correction factor W_{nm} [121] is equal to

$$W_{nm} = (r_n + r_m) \int_{r_n+r_m}^{\infty} exp\left[\frac{E(x)}{k_B T}\right] \frac{dx}{x^2} \qquad \text{Eq. 9}$$

where *x* is the distance between the particles. The van der Waals potential between the particles was modeled as described by Hamaker[123], as

$$E_{vdW}(x) = -\frac{H}{6}\left[\frac{2r_n r_m}{x^2-(r_n+r_m)^2} + \frac{2r_n r_m}{x^2-(r_n-r_m)^2} + ln\left(\frac{x^2-(r_n+r_m)^2}{x^2-(r_n-r_m)^2}\right)\right] \qquad \text{Eq. 10}$$

where H is the Hamaker constant ($8 \cdot 10^{-20}$ J for PbS[124] and $5.2 \cdot 10^{-20}$ J for the ligands[125], across vacuum, which leads to a value of $3 \cdot 10^{-21}$ for PbS across oleylamine)[54,126].

Viscous interactions describe how friction coefficients of particles approaching each other can be quite significantly different than those of isolated particles. This effect is usually accounted for by a "diffusion ratio" D^{∞}/D_{nm} that multiplies the exponential term in the integral of Equation 9. The diffusion ratio was calculated, according to Spielman[127], as

$$\frac{D^{\infty}}{D_{nm}} = 1 + \frac{2.6R_nR_m}{(R_n+R_m)^2}\sqrt{\frac{R_nR_m}{(R_n+R_m)(x-R_n-R_m)}} + \frac{R_nR_m}{(R_n+R_m)(x-R_n-R_m)} \qquad \text{Eq. 11}$$

The Coulombic interaction between the nanocrystals was neglected since zeta potential measurements indicated the absence of charges on the particles.

Lastly, the depletion interaction between particles can be quite significant in concentrated solutions[128,129]. To describe these attractive component of the interactions we used the Asakura-Oosawa model[130]

$$E_{dep,n}(x) = \sum_{\substack{i=1 \\ i\neq n}}^{p} N_i k_B T V_{dep,nm}(x) \qquad \text{Eq. 12}$$

where V_{dep} is the depletion volume created when particles approach each other. A comparison between the depletion potential and the van der Waals potential between monomers at the beginning of the reaction is shown in Figure 7c.

To account for possible inadequacies of the corrections to the collision frequency, we included in the model a size dependent correction factor $[A(r_n^B + r_m^B)]$ where A and B are fitting parameters. The resulting general kernel is

$$k_{nm} = \frac{4\pi(R_n+R_m)(D_n+D_m)}{W[A(r_n^B+r_m^B)]} exp\frac{-\left[\frac{C}{\left(\frac{1}{R_n}+\frac{1}{R_m}\right)}+D\left(r_n^E+r_m^E\right)\right]}{k_B T} \qquad \text{Eq. 13}$$

As we show in the next section, while this general model we considered initially had up to five parameters, only 2 ended up being necessary (*C* and *D*) for a good agreement with the data.

Table I. Summary of the models considered for comparison with the data

Model #	Degrees of freedom	A	B	C	D	E
		Correction to the collision frequencies		*Ligand-penetration*	*Reconstruction*	
1	1	✗	✗	✗	✓	✗
2	1	✗	✗	✓	✗	✗
3	2	✗	✗	✗	✓	✓
4	3	✗	✗	✓	✓	✓
5	4	✓	✓	✗	✓	✓
6	5	✓	✓	✓	✓	✓

Simulations of growth kinetics

Simulations of the growth kinetics were conducted with two complementary computational approaches. In one approach we solved numerically Equation 4. This approach allowed us to include the size dependence of activation energy, but it became computationally intensive when we tried to include the effect of interactions. The other approach used a finite difference approach by discretizing the process in time and calculated the change in the concentrations of each population at each discrete time point (3600 time points for a total real time of 1 hr). The separation between time points was logarithmically distributed to compensate for the larger concentrations and faster rates at early stages of reaction: the time intervals at the beginning of the reaction were as small as $6 \cdot 10^{-9}$ s. Differently from the continuum approach, this discrete approach allowed us to include straightforwardly the influence of all interactions (especially the depletion interaction).

To identify the minimum number of variables (i.e., degrees of freedom) necessary to describe the experimental data, we conducted simulations using versions of Equation 13 with different numbers and combinations of degrees of freedom, as described by Table I.

The resulting models are significantly different in the way they describe the physics of the coalescence process. Models #1 to #4 assume that the collision frequencies are adequately described by Smoluchowski's model. Model #5 and #6 instead

correct them with a size-dependent power law. In terms of rate limiting mechanisms (e.g., ligand-penetration vs reconstruction), model #1 assumes that reconstruction is the slow step but is independent of size, model #2 assumes that ligand-penetration is the slow step, models #3 and #5 assume that the reconstruction step is rate limiting but is dependent on the size of the particles, while models #4 and #6 assumes that both mechanisms proceed at similar speeds.

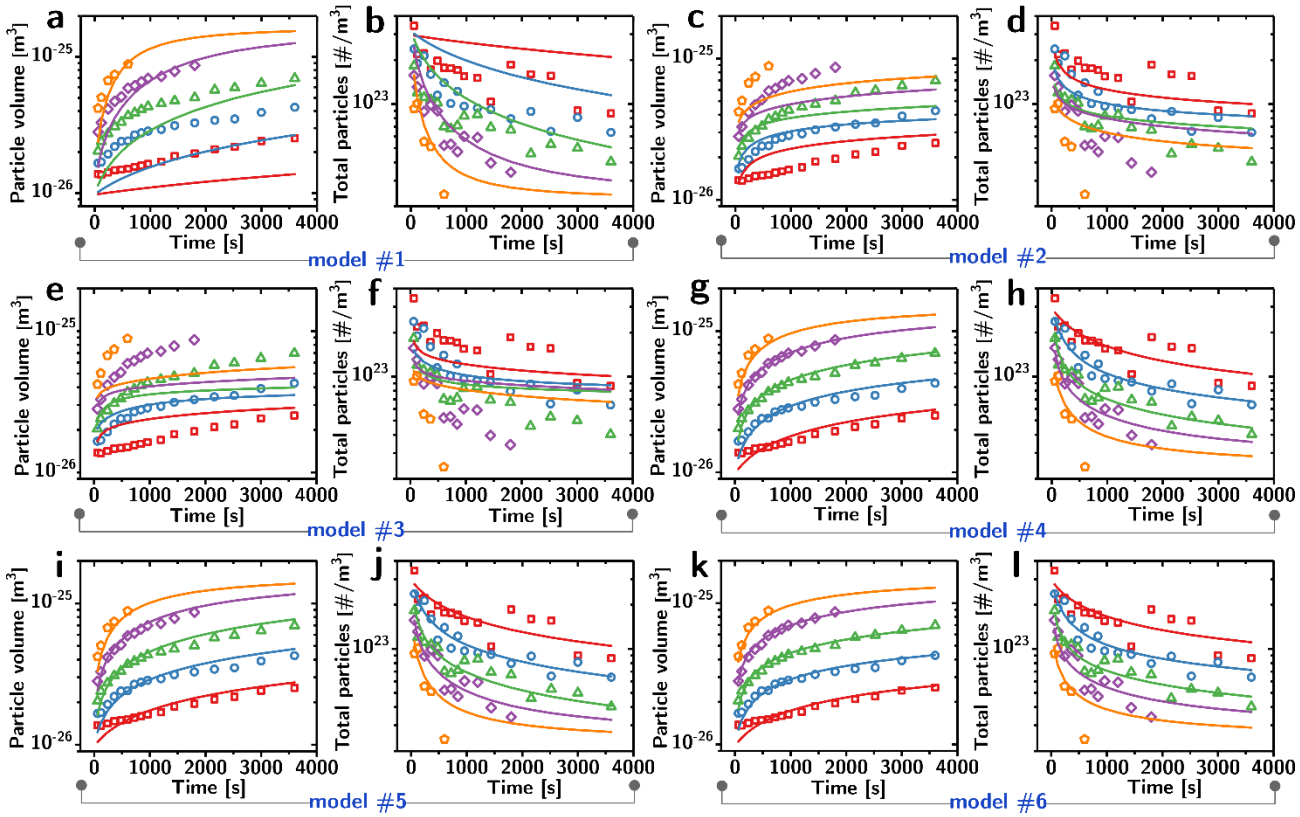

Figure 8. Comparison of simulations with experimental data for different models. This figure shows how the data of number-averaged particle volume and particle concentration (red: 80 °C, blue: 100 °C, green: 120 °C, purple: 140 °C, orange: 160 °C) are described by the six models described in the text. (a-b) model #1. (c-d) model #2. (e-f) model #3. (g-h) model #4. (i-j) model #5. (k-l) model #6.

Table II. Best fits of experimental data for the 6 models explored.

Model #	R^2 (N)	R^2 (V)	A	B	C	D	E	$\langle E_a \rangle$ *[kJ·mol⁻¹]*
1	0.21	0.58				5.2E-20		62.64
2	0.65	0.70			6.07E-11			79.84
3	0.50	0.44				2.92E-11	1	96.15
4	**0.89**	**0.99**			**2.37E-11**	**3.02E-20**	**0**	**67.65**
5	0.89	0.97	3.52E+27	3		3.99E-20	0	48.02
6	0.89	0.99	7.00	0	1.97E-11	2.64E-20	0	57.78

The comparison between the simulated and experimental data included both the total particle concentrations and the number-averaged particle volumes (each taken as a function of time and temperature). The optimal agreement between simulation and experimental data was not obtained by a least square fitting process due to concerns that it would converge to local minima in the large and complex parameter space. We instead evaluated how variances and coefficients of determination (R^2) changed in a combinatorial screening of conditions. To limit the number of possible combinations, we assumed that *B* and *E* were integers between -3 and 3.

The best fits are shown in Figure 8 while the respective values of R^2, of each fitting parameter, and of the average activation energy (in units of kJ·mol^{-1}) are listed in Table II. The fits shown in Figure 8 and listed in the Table include the corrections to the collision frequencies due to van der Waals, viscosity, and depletion interactions. Nonetheless those corrections

made only a small difference in the fits and the optimal conditions were consistent with those found by solving the system of differential equations.

The first three models fail to describe the experimental data and won't be discussed. Model #4 had the best values of R^2, and, importantly, the optimal value of the exponent *E* was found to be zero. Therefore, this model effectively has only two degrees of freedom. Model #5 obtained the third best values of R^2, but, as shown in Figure 8, it fails to accurately describe the particle volumes at long reaction times. The optimal value of E for this model was also zero, therefore reducing the number of degrees of freedom of this model to three. Model #6 obtained analogous R^2 values to #4. The optimal values for the two exponents (B and E) were zero therefore reducing the number of degrees of freedom for this model to three.

According to Ockham's razor[113,131], the model with the smallest number of degrees of freedom that adequately describes the experimental data should be considered the closest approximation to the truth.

Figure 9 shows the dependence of the values of R^2 on the effective degrees of freedom of the models, and shows how model #4 (Equation 14) appears to be the best compromise between describing accurately the data and decreasing the numbers of degrees of freedom in the model.

$$k_{nm} = \frac{4\pi(R_n+R_m)(D_n+D_m)}{W} exp \frac{-\left[\frac{C}{\left(\frac{1}{R_n}+\frac{1}{R_m}\right)}+D\right]}{k_B T} \quad \text{Eq. 14}$$

Model #4 assumes that Smoluchowski's equation adequately describes the collision frequencies and that the coalescence process is described by two terms in the activation energy: the size-dependent ligand-penetration term and a constant reconstruction term. The average ratio between those two terms is 0.86, indicating that the two processes are similarly important in determining the rate of coalescence. The fact that the reconstruction term appears to be independent of size suggests that it might be correlated to a property of PbS (e.g., bond strength). The value of the average activation energy is $1.12 \cdot 10^{-19}$ J, or 67.65 kJ·mol^{-1}. This value is consistent with prior reports in other material systems (65.5 kJ·mol^{-1} for dodecanethiol capped PbS[3], 14 kJ·mol^{-1} for thioglycerol/dithioglycerol capped PbS[70], 92 kJ·mol^{-1} for phosphinic acid-capped CdSe[6], 54.5 kJ·mol^{-1} for ZnS in 4M NaOH solution[1], 49.7 kJ·mol^{-1} for surfactant-free SnO_2[4]), but is remarkably small: it is five times smaller than the dissociation energy of the Pb-S bond[13]. While these values describe the kinetics of coalescence (and they predict the outcome of syntheses, as shown later), it is hard to believe that they correspond to the real activation energy of a process that requires the making and breaking of dozens of bonds. Further indication that the models do not perfectly capture the reality of the process lies in the polydispersity data. All models overestimated the polydispersities.

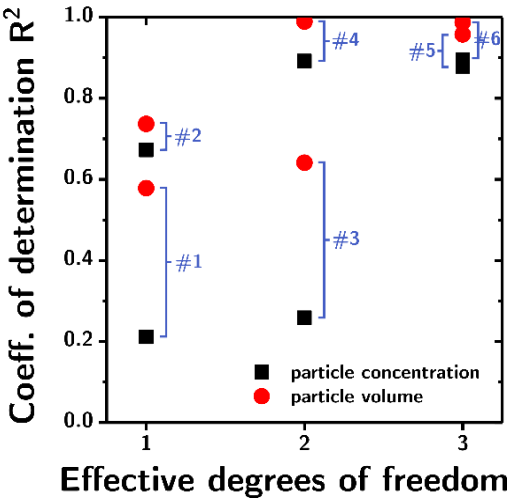

Figure 9. Model selection. This graph shows the best R^2 values obtained by each model for particle concentration (black squares) and particle volume (red circles) as a function of the effective degrees of freedom of the models.

The challenge of describing collision rates in colloidal systems

Effects of crowding and size on collision frequencies

We postulated that the general overestimation of polydispersity by all our models, and the unrealistic values of activation energy originated from an incorrect description of the collision frequencies by Smoluchowski's kernel (Equation 8). Our system is relatively crowded (particle volume fraction = ~3%; the average distance between the surfaces of the particles' ligand shells ranges between 12 and 25 nm) and the coalescence process is activated. Smoluchowski's kernel does not account for crowding effects[114]. Extensive work performed over the past few decades succeeded in correcting Smoluchowski's kernel to account for crowded systems[132-146]. Nonetheless, the work was usually focused on conditions quite different from our experiment, i.e., diffusion-limited conditions and aggregation without reconstruction. An important take home message from that body of work was that crowding significantly affected collision rates, even for relatively low volume fractions[144].

Therefore, we conducted Brownian dynamics simulations to test two mechanistic hypotheses. (i) Crowding should suppress the rate of collisions between members of rare populations by limiting the number of diffusion trajectories that can bring them into contact without colliding first with a particle from a more common population. (ii) Upon colliding, the time particles spend in contact with each other depends on their size. A depiction of these two mechanisms, which we call here respectively "traffic" and "encumbrance", is shown in Figure 10.

Traffic. Figure 10A shows two particles in close proximity and 4 diffusion trajectories that could bring the particle on the left in collision with the particle on the right (which we assume, for clarity, to be stationary). The average rates of collisions in an ensemble are a function of the number of possible collision trajectories[147]. The scenario shown in Figure 10A is the one modeled by the Smoluchowski equation: the trajectories between particles are unimpeded. The scenario in Figure 10B is

closer to our experimental system: the collision trajectories are impeded by members of other populations. Let's assume that the white particles are monomers and the black particles are dimers. Equation 14 calculates the rate constant of dimer-dimer ([22]) collisions by accounting for their collisional cross-section and diffusion constant. The rate will though be independent of the concentrations of the other populations in the system. In other words, it will not consider that a significant number of diffusional trajectories that would lead to [22] collisions in the absence of monomers cause instead dimer-monomer ([21]) collisions (and the formation of trimers, rather than the larger tetramers). The net effect should be a suppression of the rate of [22] collisions and a slower increase in polydispersity. This process should not be confused with the cage effect observed in systems close to the jamming transition where particle dynamics is slowed (i.e., a decrease in the effective diffusivity)[148].

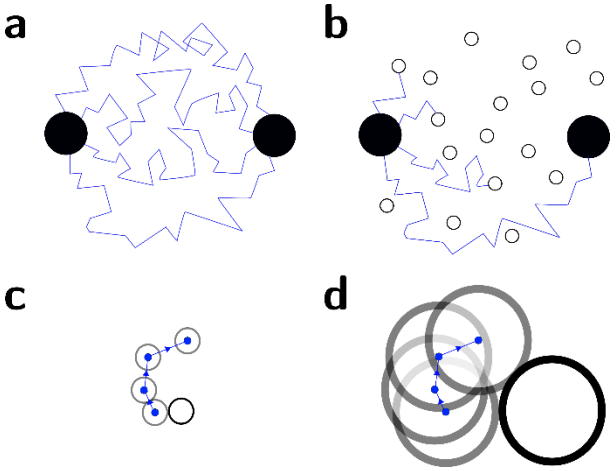

Figure 10. Traffic and encumbrance effects on collision frequencies. (a) Sketch of 4 possible diffusion trajectories (blue lines) that could cause a collision between the two black particles from the same population in the absence of particles from different populations. (b) Sketch of the same two particles and the same four trajectories in the presence of particles from a different population (white circles). (c) Sketch of a three-step trajectory bringing one particle originally in contact with another to separate. (d) Sketch of the same exact trajectory shown in panel c, but applied to larger particles, showing how the trajectory now causes the particles to recollide at the third step.

Encumbrance. Figure 10c shows two particles that are initially in contact, conducting three diffusion steps. The steps are intended to be commensurate with the diffusion mean free path of the particles,[149] which, in this case, is similar to the size of the particles themselves (as is the case for small molecules). As in the previous panels, the particle on the right is shown to be stationary for clarity. The trajectory we chose as an example causes the two particles in contact to detach and progressively increase their mutual distance. Figure 10D shows instead what happens when the diffusion trajectory is the same but the particle are significantly larger than the mean free path: the particles initially detach only to collide again. In other words, for two particles in contact, the fraction of trajectories that lead to their macroscopic separation decreases with their size. Therefore, as the particles increase in size, they spend more time in contact with each other (or, in other words, increase their collision frequency[150]).

This process should increase the rates of any process involving contact between particles, such as coalescence or oriented attachment. The Smoluchowski's equation can calculate (in non-crowded situations) the rate with which particles can come into contact with each other, but it does not account for the time they effectively stay in contact due to their mutual steric encumbrance.

Brownian dynamics simulations

To verify these hypotheses we created a Brownian dynamics simulation, similarly to the one described by Kim & Yethiraj[151]. Briefly, the particles were simulated as hard spheres. The diffusion was modeled as a random flight. The time steps equaled 1 ns, the direction of travel was randomly determined at each time step, while the distance traveled at each step was normally distributed with zero mean and variance equal to 6Dt. The RMS displacement of the particles at each time step was in the order of 2 . Given the fine time resolution and the small displacements at each step, we neglected changes in the direction of motion of the particles upon collision: colliding particles were returned to their original position.

To further limit the computational burden and allow for longer simulations, the simulated volume was a cube of 60 nm in size. Periodic boundary conditions were established by using a "ghost" particle approach[152].

Our code allowed us to pick a number of particles for each population (therefore determining concentrations). Collisions were detected by calculating the mutual distances between particles at each time step and comparing them to the sum of the respective radii.

The first set of simulations were designed to test the encumbrance hypothesis. The simulation was started with two monomers in contact with each other. They were then allowed to diffuse (time step=$1 \cdot 10^{-9}$ s, 500 steps). The duration of the simulation in real time was chosen so that the RMS displacement of the particles would be <10 nm. The simulation was run 200.000 times and each simulation was considered as a separate experiment. The probability distribution of the number of collisions in each experiment (cf. Figure 11a) shows exactly what was expected by the hypothesis. Most experiments result in a number of collisions much greater than 1. Unfortunately the distribution does not appear to be describable easily by a single exponential or by a power law, therefore compromising the estimation of an expected collision rate. The simulations were repeated by changing the size of the two particles in the simulation volume (from monomers up to decamers). The average number of collisions detected during the simulation time as a function of particle radius is shown in Figure 11b. While it does appear that the collision rate increases monotonically with the particle size, the magnitude of the uncertainty (resulting from the extremely broad probability distribution) prevents us from making claims.

With these limitations in mind, we conducted a separate set of simulations to test the traffic hypothesis. The simulation volume was filled with either 10 monomers, dimers, trimers, or hexamers (we call these particles, the "colliders"), and then

the volume fraction of the dispersion was increased by adding monomers (we dub these particles "fillers").

In this case the simulation consisted of $2 \cdot 10^6$ steps, 1 ns each (2 ms of real time). After counting the number of collisions in each simulations, we calculated the collision rate corrected by the excluded volume. Figure 11c shows the rate for monomer-monomer ([11]), dimer-dimer ([22]), trimer-trimer ([33]), and hexamer-hexamer ([66]) collisions as a function of the fraction of the simulation volume that was occupied by the particles (i.e., the volume of colliders and fillers divided by the total simulation volume). The collision rates were then normalized to the value obtained in the absence of fillers. The graph shows, as expected, that the [11] collision rates are largely unaffected by the presence of the fillers (because they are also monomers). On the other hand, the [22], [33], and [66] relative collision rates drop rapidly with an increase in the concentration of the fillers. The larger the colliders, the faster their collision rate drops with an increase in the concentration of fillers. Importantly, the range of volume fractions that we explored is similar to the one in our reaction (~3%).

In summary, the simulations confirm the intuitive prediction that the crowding of larger particles by smaller particles decreases the rate of their mutual collisions. Importantly, both of these Brownian dynamics simulations were conducted in the absence of interactions (adding interactions would make both the encumbrance and traffic effects more prominent, not less).

In this section we have shown how the analytical description of collision rate in crowded dispersion of colloidal nanoparticles is very challenging and that Smoluchowski's equation describes it incompletely. (i) The rate of collisions calculated by Equation 14 is severely underestimated because of the encumbrance effect, which causes particles to spend significant amount of time in contact due to the steric effect they have on each other's diffusion trajectories. This finding serves to explain the scarcely believable value of the activation energy obtained by the Model #4, which should be therefore only considered as an "effective" activation energy. (ii) The rate of collisions between members of rare populations is significantly lower than what predicted by the Smoluchowski's equation due to crowding by the majority populations. Both of these effects should "focus" the size distribution in a coalescing system like the one described in this work. The monomers generated at the beginning of the reaction coalesce rapidly since they are not crowded by other populations and they can trap each other. The dimers formed as a result of those collisions are instead strongly hindered from colliding with each other (forming tetramers) due to their crowding by monomers. The result should be a step-wise increase in the size of the dominant population, just as observed in the experimental data.

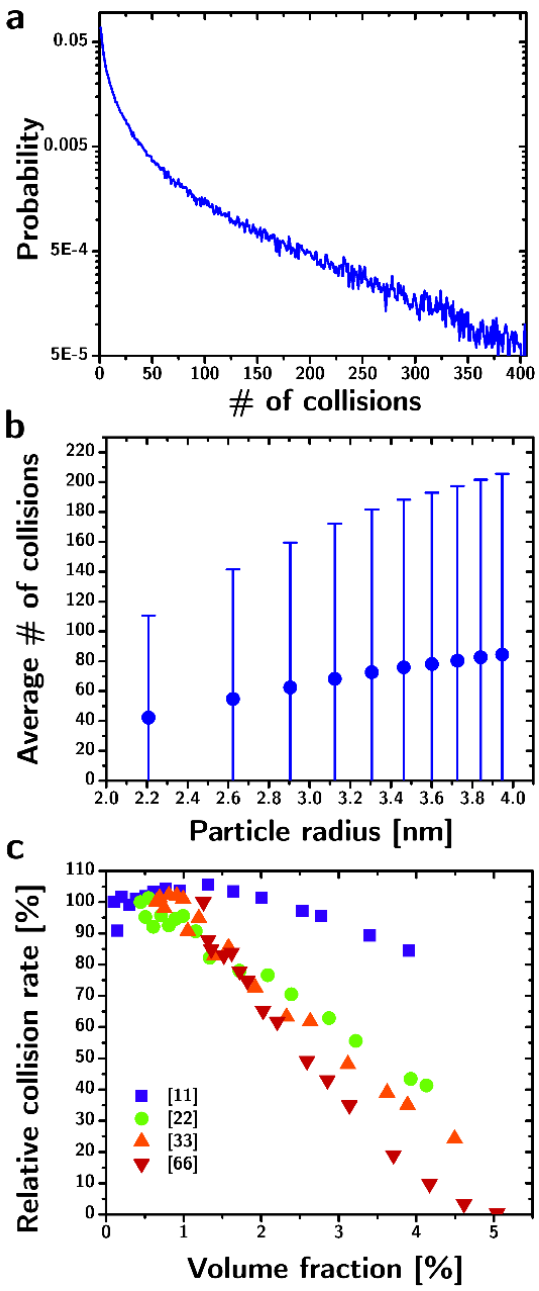

Figure 11. Brownian dynamics simulations of collision frequencies. (a) Probability distribution of the number of collisions observed between 2 particles initially in contact over the span of 500 diffusion steps. (b) Average number of collisions from the probability distribution in panel a, as a function of the size of the particles. (error bar: standard error) (c) Collision rate of a fixed concentration of monomers (blue squares), dimers (green circle), trimers (up triangle), hexamers (down triangle), as a function of the volume fraction of particles in the system (modified by adding additional monomers).

Our model predicts the growth kinetics obtained by using ligands of different lengths

The real test for any model is not so much whether it can fit experimental data but whether it can predict it. Armed with the results from our simulation of the growth kinetic of oleylamine-capped nanocrystals we wondered whether our model

could predict the growth kinetics of PbS nanocrystals capped with different ligands.

We conducted three separate reactions, using OLAHS as a sulfur precursor, and $PbCl_2$ as a lead precursor. Instead of oleylamine, each reaction used a different ligand, octadecylamine, hexadecylamine, or tetradecylamine. An amount of mesitylene was added to the reaction to reduce viscosity and facilitate sample collection. The reaction temperature was set at 120 °C, and aliquots were collected at 16 time points.

The number-averaged particle volumes and particle concentrations for each aliquot were determined as described before and are shown by the scatters in Figure 12.

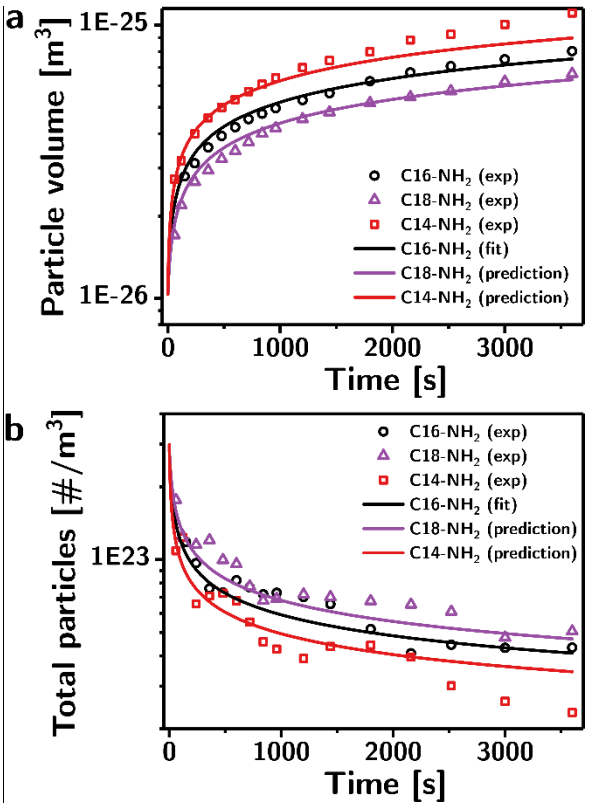

Figure 12. Prediction of growth kinetics of PbS nanocrystals capped with n-alkylamines of different lengths at 120 °C. (a) Number-averaged particle volumes as a function of time. (b) Particle concentrations as a function of time. Color coding indicates the amine ligand ($C18\text{-}NH_2$=red, $C16\text{-}NH_2$=black, $C14\text{-}NH_2$=purple). The scatters indicate the experimental data. The lines indicate results from the model (for $C16\text{-}NH_2$ the curve is a best fit, while for other ligands it is a prediction).

To predict the growth kinetics we had to find the values of the key variables, i.e., C, D, and the viscosity η. Since D is independent of particle size and temperature, we hypothesized that its value is associated with the inorganic phase. Therefore we used the optimal value of D listed in Table II. The viscosity for the amines was extrapolated from the temperature-dependent data reported in the literature[153]. The viscosity for the n-amine/mesitylene mixture was then calculated by the Grunberg and Nissan equation[154]. The interaction parameter for the mixture (necessary to solve the Grunberg and Nissan equation) was obtained from a closely related mixture (benzene/alkanes[155]) and extrapolated to 120 °C.

There was no way to predict the value of the parameter C. Therefore we used the data from the experiment with hexadecylamine to find its value ($3.09 \cdot 10^{-11}$) by fitting (black curves in Figure 12). Armed with the values of C, D, and η, we used our model to predict the growth kinetics for the octadeylamine and tetradecylamine reactions. The results are shown as the red and purple curves in Figure 12, which show excellent agreement with both the number-averaged volumes ($R^2 = 0.98$ for octadecylamine and $R^2 = 0.89$ for tetradecylamine) and concentrations ($R^2 = 0.87$ for octadecylamine and $R^2 = 0.85$ for tetradecylamine).

The value of C for the saturated amine ligands ($3.09 \cdot 10^{-11}$) is significantly larger than the value obtained from oleylamine ($2.37 \cdot 10^{-11}$), indicating that saturated ligands provide a ~80% reduction in the rate of aggregation, when compared to mono-unsaturated ones of equal length.

Conclusions

We have shown how coalescence can be a significant mechanism of growth for colloidal nanocrystals in solution, even when they are sterically stabilized by ligands. In summary, our main conclusions are as follows.

Coalescence between ligand-capped nanocrystals can happen at rates comparable to bimolecular reactions. The average rates of coalescence with oleylamine as a capping ligand (10^{-2} to 10^{1} $M^{-1} \cdot s^{-1}$) were comparable to those observed in the end-to-end coupling of Bi_2S_3 colloidal nanowires ($4 \cdot 10^{3}$ $M^{-1} \cdot s^{-1}$), and are within the range of characteristic bimolecular reaction rates (from ~10^{-5} $M^{-1} \cdot s^{-1}$ in step-growth polymerization[156] to ~10^{5} $M^{-1} \cdot s^{-1}$ in diffusion-controlled coupling[157,158]). The lack of coalescence in the control experiment is explained by the lower concentration of particles ($2.5 \cdot 10^{-2}$ mM vs 0.5 mM, resulting in a 400-fold decrease in the rate of coalescence). These rates of coalescence suggest the tantalizing possibility that colloid-colloid "reactions" that could mimic bimolecular reactions might have been overlooked because of the relatively low concentrations of nanocrystals commonly used in nanocrystal chemistry (typically <10^{-5} M, which would results in rates of aggregation ~100 slower than in our synthesis).

The rates can be described quantitatively and predicted. Our model successfully describes and predict experimental data by introducing a size-dependence to the activation energy that is proportional to contact area between ligand shells. We attribute this term of the activation energy to the process of penetrating the ligand shell. Our model does not make assumptions based on the composition of the nanoparticles, which suggest that it might be generally applicable to other materials.

Saturated ligands appear to reduce the rate of aggregation by 80% when compared to mono-unsaturated ligands. The model works equally well for saturated and unsaturated ligands. The difference in the activation energies between these two types of ligands indicate that saturated ligands are 80% more likely to prevent coalescence in a typical collision, possibly due to increased ligand-ligand interactions within the shell.

Aggregation-driven growth does not need to increase polydispersity. We have shown that aggregation-driven growth

does not necessarily increase polydispersity because (i) it can result in coalescence (i.e., reconstruction of the particle into an isotropic shape), and (ii) the rates of coalescence can be strongly dependent on particle size. This realization suggest the remarkable possibility of using coalescence as a highly sustainable and scalable particle growth process requiring minimal chemical input (i.e. coalescence that takes place significantly at high concentration of particles).

The activation energies obtained from the model are, most likely, "effective" and result from an inaccurate description of the collision frequencies. The values of the average activation energies we have obtained from the model (67.65 $kJ \cdot mol^{-1}$) are consistent with prior literature but are not credible if taken at face value. They suggest that a process as complex as the penetration of a ligand shell and the reconstruction of an entire nanocrystal has a net energy cost that is 5 times smaller than the binding energy between the Pb and S atoms. Nonetheless, these activation energies and the resulting rates explain and predict experimental data. Our explanation is that these values of activation energy are "effective" and result from an incorrect modeling of collision rates.

Smoluchowski's model is inadequate in describing the collisional frequencies in crowded colloidal dispersions. We have shown how the Smoluchowski's model for collision rates neglects at least two fundamental processes that are characteristic of Brownian diffusion of colloids in crowded dispersions. We have called these two processes "encumbrance" and "traffic". The encumbrance mechanism significantly increases the time particles spends in proximity of each other between their initial collision and their separation back into the bulk solution. The mutual steric encumbrance of the particles and their large size compared to their mean free path of diffusion limit the number of trajectories that lead them to separate. The traffic mechanism instead shows that the collisions [jj] between members of a rare population j is severely suppressed by the presence of members of a common population i. Most trajectories that would lead to [jj] collisions in the absence of i particles result instead in [ij] collisions.

It might not be possible to conduct fully ab-initio predictions of growth kinetics in ensembles of crystals in solution. The fundamental problem of describing the kinetics of these collisions lies in the extremely long tail of the distribution of residence times of particles in contact with each other. These tails have disproportionate effect on the average kinetics of the system, and could possibly be extremely sensitive to experimental parameters. In such case, the extraction of the "real" activation energies of coalescence could prove elusive.

The Ostwald ripening equation is not diagnostic. As we have shown in this work, the Ostwald ripening equation is sufficiently vague and flexible to allow for the fitting of growth kinetics resulting from completely different non-ripening processes (addition-based classical crystallization in the presence of supersaturation as well as aggregation-driven growth in the absence of supersaturation). We believe Ostwald ripening should only be claimed when other mechanisms have been disproven, on the basis of the principle of the "burden of disproof"[9]. In many occasions, aggregation-driven growth processes are likely to have been misinterpreted in the past as Ostwald ripening.

Electron microscopy cannot easily disprove aggregation-driven growth. We have shown in this work how the coalescence of small monomer particles results in differences in diameter between "neighboring" populations (e.g., hexamers vs heptamers) that are smaller than the resolution of most imaging platforms. Even if the resolution of imaging is at the single atom level, one has to account for the errors associated with the conversion of diameter/area information into volume, and the necessity of very significant sample sizes to rigorously disprove the multimodality of a distribution.

Accurate information on the temperature-dependent viscosities of the reaction media is essential to model growth kinetics. One often overlooked variable in studies of aggregation is viscosity, which plays a very significant role in determining the diffusivity of the particles. For studies of this kind to become increasingly quantitative it is essential to have reliable data on viscosities, especially when complex mixtures are used.

This paper shows how the exceptional optical properties of colloidal quantum dots provide unique opportunities for the study of crystal growth kinetics in ensembles of crystals, and the elucidation of complex effects (e.g., steric stabilization by ligands, crowding).

ASSOCIATED CONTENT

Supporting Information. Materials and methods. This material is available free of charge via the Internet at http://pubs.acs.org.

AUTHOR INFORMATION

Corresponding Author

* ludovico.cademartiri@unipr.it

Author Contributions

LC designed the study. BY conducted sample characterizations. LC and BY jointly conducted the syntheses, developed the simulations, analyzed the data, and wrote the paper.

Funding Sources

This work was supported by MSR-Intel program of Semiconductor Research Corporation under Award No. 2015-IN-2582.

ACKNOWLEDGMENT

We are grateful for generous support of this work by MSR-Intel program of Semiconductor Research Corporation under Award No. 2015-IN-2582. The authors thank Matthew G. Panthani for providing access to a UV–Vis–NIR spectrometer, and Alberto Passalacqua for insightful discussions.

ABBREVIATIONS

OLAHS, oleylammonium hydrosulfide; TEM, transmission electron microscopy; XRD, x-ray diffraction; ICP-AES, inductively coupled plasma atomic emission spectroscopy; TGA, thermal gravimetric analysis.

REFERENCES

(1) Zhang, J.; Lin, Z.; Lan, Y.; Ren, G.; Chen, D.; Huang, F.; Hong, M. A multistep oriented attachment kinetics: coarsening of ZnS nanoparticle in concentrated NaOH. *J. Am. Chem. Soc.* **2006**, *128*, 12981.
(2) Xue, X. G.; Penn, R. L.; Leite, E. R.; Huang, F.; Lin, Z. Crystal growth by oriented attachment: kinetic models and control factors. *CrystEngComm* **2014**, *16*, 1419.
(3) Zhang, J.; Wang, Y.; Zheng, J.; Huang, F.; Chen, D.; Lan, Y.; Ren, G.; Lin, Z.; Wang, C. Oriented attachment kinetics for ligand capped nanocrystals: Coarsening of thiol-PbS nanoparticles. *J. Phys. Chem. B* **2007**, *111*, 1449.
(4) Zhuang, Z. Y.; Zhang, J.; Huang, F.; Wang, Y. H.; Lin, Z. Pure multistep oriented attachment growth kinetics of surfactant-free SnO2 nanocrystals. *Phys. Chem. Chem. Phys.* **2009**, *11*, 8516.
(5) Huang, F.; Zhang, H. Z.; Banfield, J. F. Two-stage crystal-growth kinetics observed during hydrothermal coarsening of nanocrystalline ZnS. *Nano Lett.* **2003**, *3*, 373.
(6) Evans, C. M.; Love, A. M.; Weiss, E. A. Surfactant-Controlled Polymerization of Semiconductor Clusters to Quantum Dots through Competing Step-Growth and Living Chain-Growth Mechanisms. *J. Am. Chem. Soc.* **2012**, *134*, 17298.
(7) Smoluchowski, M. V. Drei Vortrage uber Diffusion, Brownsche Bewegung und Koagulation von Kolloidteilchen. *Phys. Z.* **1916**, *17*, 557.
(8) Peng, X. G.; Wickham, J.; Alivisatos, A. P. Kinetics of II-VI and III-V colloidal semiconductor nanocrystal growth: "Focusing" of size distributions. *J. Am. Chem. Soc.* **1998**, *120*, 5343.
(9) Scott, S. L. The Burden of Disproof. *ACS Catalysis* **2019**, *9*, 4706.
(10) Shields, S. P.; Richards, V. N.; Buhro, W. E. Nucleation control of size and dispersity in aggregative nanoparticle growth. A study of the coarsening kinetics of thiolate-capped gold nanocrystals. *Chem. Mater.* **2010**, *22*, 3212.
(11) Zheng, H. M.; Smith, R. K.; Jun, Y. W.; Kisielowski, C.; Dahmen, U.; Alivisatos, A. P. Observation of Single Colloidal Platinum Nanocrystal Growth Trajectories. *Science* **2009**, *324*, 1309.
(12) Flory, P. J. *Principles of Polymer Chemistry*; Cornell University Press: Ithaca, 1969.
(13) *Lange's Handbook of Chemistry*; 15th ed.; McGraw-Hill, 1999.
(14) Park, J.; Joo, J.; Kwon, S. G.; Jang, Y.; Hyeon, T. Synthesis of monodisperse spherical nanocrystals. *Angew. Chem. Int. Edit.* **2007**, *46*, 4630.
(15) Wang, T.; Zhu, Y.; Zhang, S.; Tang, H.; Wang, H. Grain morphology evolution behavior of titanium alloy components during laser melting deposition additive manufacturing. *J. Alloys Compd.* **2015**, *632*, 505.
(16) Li, D. S.; Nielsen, M. H.; Lee, J. R. I.; Frandsen, C.; Banfield, J. F.; De Yoreo, J. J. Direction-Specific Interactions Control Crystal Growth by Oriented Attachment. *Science* **2012**, *336*, 1014.
(17) Gebauer, D.; Volkel, A.; Cölfen, H. Stable Prenucleation Calcium Carbonate Clusters. *Science* **2008**, *322*, 1819.
(18) Yuwono, V. M.; Burrows, N. D.; Soltis, J. A.; Penn, R. L. Oriented Aggregation: Formation and Transformation of Mesocrystal Intermediates Revealed. *J. Am. Chem. Soc.* **2010**, *132*, 2163.
(19) Cademartiri, L.; Guerin, G.; Bishop, K. J. M.; Winnik, M. A.; Ozin, G. A. Polymer-like Conformation and Growth Kinetics of Bi2S3 Nanowires. *J. Am. Chem. Soc.* **2012**, *134*, 9327.
(20) Tang, Z.; Kotov, N. A.; Giersig, M. Spontaneous organization of single CdTe nanoparticles into luminescent nanowires. *Science* **2002**, *297*, 237.
(21) Murray, C. B.; Norris, D. J.; Bawendi, M. G. Synthesis and characterization of nearly monodisperse CdE (E = sulfur, selenium, tellurium) semiconductor nanocrystallites. *J. Am. Chem. Soc.* **1993**, *115*, 8706.
(22) Peng, X.; Manna, L.; Yang, W.; Wickham, J.; Scher, E.; Kadavanich, A.; Alivisatos, A. P. Shape control of CdSe nanocrystals. *Nature* **2000**, *404*, 59.
(23) Manna, L.; Scher, E. C.; Alivisatos, A. P. Synthesis of Soluble and Processable Rod-, Arrow-, Teardrop-, and Tetrapod-Shaped CdSe Nanocrystals. *J. Am. Chem. Soc.* **2000**, *122*, 12700.
(24) Stach, E. A.; Pauzauskie, P. J.; Kuykendall, T.; Goldberger, J.; He, R. R.; Yang, P. D. Watching GaN nanowires grow. *Nano Lett.* **2003**, *3*, 867.
(25) Manna, L.; Milliron, D. J.; Meisel, A.; Scher, E. C.; Alivisatos, A. P. Controlled growth of tetrapod-branched inorganic nanocrystals. *Nat. Mater.* **2003**, *2*, 382.
(26) Cho, K. S.; Talapin, D. V.; Gaschler, W.; Murray, C. B. Designing PbSe nanowires and nanorings through oriented attachment of nanoparticles. *J. Am. Chem. Soc.* **2005**, *127*, 7140.
(27) Lu, X.; Yavuz, M. S.; Tuan, H.-Y.; Korgel, B. A.; Xia, Y. Ultrathin Gold Nanowires Can Be Obtained by Reducing Polymeric Strands of Oleylamine:AuCl Complexes Formed via Aurophilic Interaction. *J. Am. Chem. Soc.* **2008**, *130*, 8900.
(28) Cölfen, H.; Antonietti, M. *Mesocrystals and Nonclassical Crystallization*; John Wiley & Sons: West Sussex, UK, 2008.
(29) Belcher, A. M.; Wu, X. H.; Christensen, R. J.; Hansma, P. K.; Stucky, G. D.; Morse, D. E. Control of crystal phase switching and orientation by soluble mollusc-shell proteins. *Nature* **1996**, *381*, 56.
(30) Aizenberg, J.; Black, A. J.; Whitesides, G. M. Control of crystal nucleation by patterned self-assembled monolayers. *Nature* **1999**, *398*, 495.
(31) Aizenberg, J.; Muller, D. A.; Grazul, J. L.; Hamann, D. Direct fabrication of large micropatterned single crystals. *Science* **2003**, *299*, 1205.
(32) Matthews, J. *Epitaxial growth*; Elsevier, 2012.
(33) Canfield, P. C.; Fisk, Z. Growth of single crystals from metallic fluxes. *Philos. Mag. B* **1992**, *65*, 1117.
(34) Barrett, D.; McHugh, J.; Hobgood, H.; Hopkins, R.; McMullin, P.; Clarke, R.; Choyke, W. Growth of large SiC single crystals. *J. Cryst. Growth* **1993**, *128*, 358.
(35) LaMer, V. K.; Dinegar, R. H. Theory, Production and Mechanism of Formation of Monodispersed Hydrosols. *J. Am. Chem. Soc.* **1950**, *72*, 4847.
(36) Thanh, N. T.; Maclean, N.; Mahiddine, S. Mechanisms of nucleation and growth of nanoparticles in solution. *Chem. Rev.* **2014**, *114*, 7610.
(37) Reiss, H. The growth of uniform colloidal dispersions. *J. Chem. Phys.* **1951**, *19*, 482.
(38) Kwon, S. G.; Hyeon, T. Formation mechanisms of uniform nanocrystals via hot-injection and heat-up methods. *Small* **2011**, *7*, 2685.
(39) Murray, C. B.; Norris, D. J.; Bawendi, M. G. Synthesis and Characterization of Nearly Monodisperse Cde (E = S, Se, Te) Semiconductor Nanocrystallites. *J. Am. Chem. Soc.* **1993**, *115*, 8706.
(40) Kwon, S. G.; Piao, Y.; Park, J.; Angappane, S.; Jo, Y.; Hwang, N.-M.; Park, J.-G.; Hyeon, T. Kinetics of monodisperse iron oxide nanocrystal formation by "heating-up" process. *J. Am. Chem. Soc.* **2007**, *129*, 12571.

(41) van Embden, J.; Chesman, A. S.; Jasieniak, J. J. The heat-up synthesis of colloidal nanocrystals. *Chem. Mater.* **2015**, *27*, 2246.
(42) De Yoreo, J. J.; Vekilov, P. G. Principles of crystal nucleation and growth. *Rev. Mineral. Geochem.* **2003**, *54*, 57.
(43) Voorhees, P. W. THE THEORY OF OSTWALD RIPENING. *J. Stat. Phys.* **1985**, *38*, 231.
(44) Ostwald, W. *Lehrbuch der Allgemeinen Chemie* Leipzig, Germany, 1896; Vol. 2.
(45) Gebauer, D.; Raiteri, P.; Gale, J. D.; Cölfen, H. On classical and non-classical views on nucleation. *Am. J. Sci.* **2018**, *318*, 969.
(46) Merikanto, J.; Zapadinsky, E.; Lauri, A.; Vehkamäki, H. Origin of the failure of classical nucleation theory: Incorrect description of the smallest clusters. *Phys. Rev. Lett.* **2007**, *98*, 145702.
(47) Fladerer, A.; Strey, R. Homogeneous nucleation and droplet growth in supersaturated argon vapor: The cryogenic nucleation pulse chamber. *J. Chem. Phys.* **2006**, *124*, 164710.
(48) Laaksonen, A.; Napari, I. Breakdown of the capillarity approximation in binary nucleation: a density functional study. *J. Phys. Chem. B* **2001**, *105*, 11678.
(49) Djikaev, Y.; Bowles, R.; Reiss, H. Role of constraints in the thermodynamics of heterogeneous condensation on solid soluble particles: failure of the capillarity approximation. *Physica A* **2001**, *298*, 155.
(50) Kwon, G.; Sung, B. J.; Yethiraj, A. Dynamics in crowded environments: is non-Gaussian Brownian diffusion normal? *J. Phys. Chem. B* **2014**, *118*, 8128.
(51) Dix, J. A.; Verkman, A. Crowding effects on diffusion in solutions and cells. *Annu. Rev. Biophys.* **2008**, *37*, 247.
(52) Boles, M. A.; Ling, D.; Hyeon, T.; Talapin, D. V. The surface science of nanocrystals. *Nat. Mater.* **2016**, *15*, 141.
(53) Bishop, K. J. M.; Wilmer, C. E.; Soh, S.; Grzybowski, B. A. Nanoscale Forces and Their Uses in Self-Assembly. *Small* **2009**, 5, 1600.
(54) Israelachvili, J. N. *Intermolecular and surface forces*; Academic press, 2015.
(55) Penn, R. L.; Banfield, J. F. Imperfect oriented attachment: dislocation generation in defect-free nanocrystals. *Science* **1998**, *281*, 969.
(56) Liao, H.-G.; Cui, L.; Whitelam, S.; Zheng, H. Real-time imaging of Pt3Fe nanorod growth in solution. *Science* **2012**, *336*, 1011.
(57) Banfield, J. F.; Welch, S. A.; Zhang, H. Z.; Ebert, T. T.; Penn, R. L. Aggregation-based crystal growth and microstructure development in natural iron oxyhydroxide biomineralization products. *Science* **2000**, *289*, 751.
(58) Lee, J.; Yang, J.; Kwon, S. G.; Hyeon, T. Nonclassical nucleation and growth of inorganic nanoparticles. *Nat. Rev. Mater.* **2016**, *1*, 16034.
(59) Wang, F.; Richards, V. N.; Shields, S. P.; Buhro, W. E. Kinetics and mechanisms of aggregative nanocrystal growth. *Chem. Mater.* **2013**, *26*, 5.
(60) Richards, V. N.; Rath, N. P.; Buhro, W. E. Pathway from a molecular precursor to silver nanoparticles: the prominent role of aggregative growth. *Chem. Mater.* **2010**, *22*, 3556.
(61) Huang, F.; Zhang, H. Z.; Banfield, J. F. The role of oriented attachment crystal growth in hydrothermal coarsening of nanocrystalline ZnS. *J. Phys. Chem. B* **2003**, *107*, 10470.
(62) Bogush, G.; Zukoski Iv, C. Uniform silica particle precipitation: an aggregative growth model. *J. Colloid Interface Sci.* **1991**, *142*, 19.
(63) Yin, S.; Huang, F.; Zhang, J.; Zheng, J.; Lin, Z. The effects of particle concentration and surface charge on the oriented attachment growth kinetics of CdTe nanocrystals in H2O. *J. Phys. Chem. C* **2011**, *115*, 10357.
(64) Richards, V. N.; Shields, S. P.; Buhro, W. E. Nucleation control in the aggregative growth of bismuth nanocrystals. *Chem. Mater.* **2010**, *23*, 137.
(65) Baumgartner, J.; Dey, A.; Bomans, P. H.; Le Coadou, C.; Fratzl, P.; Sommerdijk, N. A.; Faivre, D. Nucleation and growth of magnetite from solution. *Nature materials* **2013**, *12*, 310.
(66) Ribeiro, C.; Lee, E. J. H.; Longo, E.; Leite, E. R. A kinetic model to describe nanocrystal growth by the oriented attachment mechanism. *ChemPhysChem* **2005**, *6*, 690.
(67) Brauser, E. M.; Hull, T. D.; McLennan, J. D.; Siy, J. T.; Bartl, M. H. Experimental evaluation of kinetic and thermodynamic reaction parameters of colloidal nanocrystals. *Chem. Mater.* **2016**, *28*, 3831.
(68) Ribeiro, C.; Lee, E. J. H.; Longo, E.; Leite, E. R. Oriented attachment mechanism in anisotropic nanocrystals: A "polymerization" approach. *ChemPhysChem* **2006**, *7*, 664.
(69) Van Hyning, D. L.; Klemperer, W. G.; Zukoski, C. F. Silver nanoparticle formation: predictions and verification of the aggregative growth model. *Langmuir* **2001**, *17*, 3128.
(70) Brazeau, A. L.; Jones, N. D. Growth Mechanisms in Nanocrystalline Lead Sulfide by Stopped-Flow Kinetic Analysis. *J. Phys. Chem. C* **2009**, *113*, 20246.
(71) Ratkovich, A. S.; Penn, R. L. Controlling nanosized ZnO growth kinetics using various Zn: OH concentration ratios. *J. Phys. Chem. C* **2007**, *111*, 14098.
(72) Burrows, N. D.; Hale, C. R. H.; Penn, R. L. Effect of Ionic Strength on the Kinetics of Crystal Growth by Oriented Aggregation. *Cryst. Growth Des.* **2012**, *12*, 4787.
(73) Burrows, N. D.; Hale, C. R. H.; Penn, R. L. Effect of pH on the Kinetics of Crystal Growth by Oriented Aggregation. *Cryst. Growth Des.* **2013**, *13*, 3396.
(74) Penn, R. L.; Tanaka, K.; Erbs, J. Size dependent kinetics of oriented aggregation. *J. Cryst. Growth* **2007**, *309*, 97.
(75) Libert, S.; Gorshkov, V.; Goia, D.; Matijević, E.; Privman, V. Model of controlled synthesis of uniform colloid particles: cadmium sulfide. *Langmuir* **2003**, *19*, 10679.
(76) Wang, Y.; Zhang, J.; Yang, Y.; Huang, F.; Zheng, J.; Chen, D.; Yan, F.; Lin, Z.; Wang, C. NaOH concentration effect on the oriented attachment growth kinetics of ZnS. *J. Phys. Chem. B* **2007**, *111*, 5290.
(77) Drews, T. O.; Katsoulakis, M. A.; Tsapatsis, M. A mathematical model for crystal growth by aggregation of precursor metastable nanoparticles. *J. Phys. Chem. B* **2005**, *109*, 23879.
(78) Drews, T. O.; Tsapatsis, M. Model of the evolution of nanoparticles to crystals via an aggregative growth mechanism. *Microporous Mesoporous Mater.* **2007**, *101*, 97.
(79) Liao, H.-G.; Zheng, H. Liquid cell transmission electron microscopy study of platinum iron nanocrystal growth and shape evolution. *J. Am. Chem. Soc.* **2013**, *135*, 5038.
(80) Yuk, J. M.; Park, J.; Ercius, P.; Kim, K.; Hellebusch, D. J.; Crommie, M. F.; Lee, J. Y.; Zettl, A.; Alivisatos, A. P. High-resolution EM of colloidal nanocrystal growth using graphene liquid cells. *Science* **2012**, *336*, 61.
(81) Wang, W.; Banerjee, S.; Jia, S.; Steigerwald, M. L.; Herman, I. P. Ligand control of growth, morphology, and capping structure of colloidal CdSe nanorods. *Chem. Mater.* **2007**, *19*, 2573.
(82) Narayanaswamy, A.; Xu, H.; Pradhan, N.; Kim, M.; Peng, X. Formation of nearly monodisperse In2O3 nanodots and oriented-attached nanoflowers: hydrolysis and alcoholysis vs pyrolysis. *J. Am. Chem. Soc.* **2006**, *128*, 10310.
(83) Dagtepe, P.; Chikan, V.; Jasinski, J.; Leppert, V. J. Quantized growth of CdTe quantum dots; observation of

magic-sized CdTe quantum dots. *J. Phys. Chem. C* **2007**, *111*, 14977.
(84) de Mello Donegá, C. Synthesis and properties of colloidal heteronanocrystals. *Chem. Soc. Rev.* **2011**, *40*, 1512.
(85) Houtepen, A. J.; Koole, R.; Vanmaekelbergh, D.; Meeldijk, J.; Hickey, S. G. The hidden role of acetate in the PbSe nanocrystal synthesis. *J. Am. Chem. Soc.* **2006**, *128*, 6792.
(86) Lee, E. J.; Ribeiro, C.; Longo, E.; Leite, E. R. Growth kinetics of tin oxide nanocrystals in colloidal suspensions under hydrothermal conditions. *Chem. Phys.* **2006**, *328*, 229.
(87) Yuk, J. M.; Jeong, M.; Kim, S. Y.; Seo, H. K.; Kim, J.; Lee, J. Y. In situ atomic imaging of coalescence of Au nanoparticles on graphene: rotation and grain boundary migration. *Chem. Comm.* **2013**, *49*, 11479.
(88) Yuan, B.; Egner, T. K.; Venditti, V.; Cademartiri, L. Sustainable scalable synthesis of sulfide nanocrystals at low cost with an ionic liquid sulfur precursor. *Nat. Commun.* **2018**, *9*, 4078.
(89) Cademartiri, L.; Bertolotti, J.; Sapienza, R.; Wiersma, D. S.; Kitaev, V.; Ozin, G. A. Multigram Scale, Solventless and Diffusion-Controlled Route to Highly Monodisperse PbS Nanocrystals. *J. Phys. Chem. B* **2006**, *110*, 671.
(90) Cademartiri, L.; Ozin, G. A. Emerging strategies for the synthesis of highly monodisperse colloidal nanostructures. *Philos. Trans. R. Soc. London, A* **2010**, *368*, 4229.
(91) Thomson, J. W.; Nagashima, K.; Macdonald, P. M.; Ozin, G. A. From Sulfur-Amine Solutions to Metal Sulfide Nanocrystals: Peering into the Oleylamine-Sulfur Black Box. *J. Am. Chem. Soc.* **2011**, *133*, 5036.
(92) Langford, J. I.; Wilson, A. J. C. Sherrer after Sixty Years: A Survey and Some New Results in the Determination of Crystallite Size. *J. Appl. Crystallogr.* **1978**, *11*, 102.
(93) Mohapatra, P.; Shaw, S.; Mendivelso-Perez, D.; Bobbitt, J. M.; Silva, T. F.; Naab, F.; Yuan, B.; Tian, X.; Smith, E. A.; Cademartiri, L. Calcination does not remove all carbon from colloidal nanocrystal assemblies. *Nat. Commun.* **2017**, *8*, 2038.
(94) Yu, W. W.; Qu, L.; Guo, W.; Peng, X. Experimental Determination of the Extinction Coefficient of CdTe, CdSe, and CdS Nanocrystals. *Chem. Mater.* **2003**, *15*, 2854.
(95) Cademartiri, L.; Montanari, E.; Calestani, G.; Migliori, A.; Guagliardi, A.; Ozin, G. A. Size-dependent extinction coefficients of PbS quantum dots. *J. Am. Chem. Soc.* **2006**, *128*, 10337.
(96) Wise, F. W. Lead Salt Quantum Dots: the Limit of Strong Quantum Confinement. *Acc. Chem. Res.* **2000**, *33*, 773.
(97) Moreels, I.; Lambert, K.; Smeets, D.; De Muynck, D.; Nollet, T.; Martins, J. C.; Vanhaecke, F.; Vantomme, A.; Delerue, C.; Allan, G.; Hens, Z. Size-Dependent Optical Properties of Colloidal PbS Quantum Dots. *ACS Nano* **2009**, *3*, 3023.
(98) Norris, D. J.; Bawendi, M. G. Measurement and assignment of the size-dependent optical spectrum in CdSe quantum dots. *Phys. Rev. B: Condens. Matter* **1996**, *53*, 16338.
(99) Sun, J. J.; Goldys, E. M. Linear absorption and molar extinction coefficients in direct semiconductor quantum dots. *J. Phys. Chem. C* **2008**, *112*, 9261.
(100) Hendricks, M. P.; Campos, M. P.; Cleveland, G. T.; Jen-La Plante, I.; Owen, J. S. A tunable library of substituted thiourea precursors to metal sulfide nanocrystals. *Science* **2015**, *348*, 1226.
(101) Penn, R. L. Kinetics of oriented aggregation. *J. Phys. Chem. B* **2004**, *108*, 12707.
(102) Meldrum, F. C.; Cölfen, H. Controlling mineral morphologies and structures in biological and synthetic systems. *Chem. Rev.* **2008**, *108*, 4332.
(103) Williamson, C. B.; Nevers, D. R.; Hanrath, T.; Robinson, R. D. Prodigious Effects of Concentration Intensification on Nanoparticle Synthesis: A High-Quality, Scalable Approach. *J. Am. Chem. Soc.* **2015**, *137*, 15843.
(104) Zhang, H.; Hyun, B.-R.; Wise, F. W.; Robinson, R. D. A Generic Method for Rational Scalable Synthesis of Monodisperse Metal Sulfide Nanocrystals. *Nano Lett.* **2012**, *12*, 5856.
(105) Kan, S.; Mokari, T.; Rothenberg, E.; Banin, U. Synthesis and size-dependent properties of zinc-blende semiconductor quantum rods. *Nat. Mater.* **2003**, *2*, 155.
(106) Andreev, A. D.; Lipovskii, A. A. Anisotropy-induced optical transitions in PbSe and PbS spherical quantum dots. *Phys. Rev. B: Condens. Matter Mater. Phys.* **1999**, *59*, 15402.
(107) De Yoreo, J. J.; Gilbert, P. U.; Sommerdijk, N. A.; Penn, R. L.; Whitelam, S.; Joester, D.; Zhang, H.; Rimer, J. D.; Navrotsky, A.; Banfield, J. F. Crystallization by particle attachment in synthetic, biogenic, and geologic environments. *Science* **2015**, *349*, aaa6760.
(108) De Yoreo, J. J.; Sommerdijk, N. A. Investigating materials formation with liquid-phase and cryogenic TEM. *Nat. Rev. Mater.* **2016**, *1*, 16035.
(109) De Yoreo, J. J.; Gilbert, P. U.; Sommerdijk, N. A.; Penn, R. L.; Whitelam, S.; Joester, D.; Zhang, H.; Rimer, J. D.; Navrotsky, A.; Banfield, J. F. Crystallization by particle attachment in synthetic, biogenic, and geologic environments. *Science* **2015**, *349*.
(110) Massey Jr, F. J. The Kolmogorov-Smirnov test for goodness of fit. *J. Am. Stat. Assoc.* **1951**, *46*, 68.
(111) Liu, K.; Nie, Z.; Zhao, N.; Li, W.; Rubinstein, M.; Kumacheva, E. Step-growth polymerization of inorganic nanoparticles. *Science* **2010**, *329*, 197.
(112) Talapin, D. V.; Rogach, A. L.; Haase, M.; Weller, H. Evolution of an ensemble of nanoparticles in a colloidal solution: Theoretical study. *J. Phys. Chem. B* **2001**, *105*, 12278.
(113) Vandekerckhove, J.; Matzke, D.; Wagenmakers, E.-J. Model comparison and the principle of parsimony. *Oxford handbook of computational and mathematical psychology* **2015**, 300.
(114) Ramkrishna, D. Population balances: Theory and applications to particulate systems in engineering; Elsevier, 2000.
(115) Milner, S. T.; Witten, T.; Cates, M. Theory of the grafted polymer brush. *Macromolecules* **1988**, *21*, 2610.
(116) Geva, N.; Shepherd, J. J.; Nienhaus, L.; Bawendi, M. G.; Van Voorhis, T. Morphology of passivating organic ligands around a nanocrystal. *J. Phys. Chem. C* **2018**, *122*, 26267.
(117) Shaw, S.; Yuan, B.; Tian, X. C.; Miller, K. J.; Cote, B. M.; Colaux, J. L.; Migliori, A.; Panthani, M. G.; Cademartiri, L. Building Materials from Colloidal Nanocrystal Arrays: Preventing Crack Formation During Ligand Removal by Controlling Structure and Solvation. *Advanced Materials* **2016**, *28*, 8892.
(118) Valdez, C. N.; Schimpf, A. M.; Gamelin, D. R.; Mayer, J. M. Low capping group surface density on zinc oxide nanocrystals. *ACS Nano* **2014**, *8*, 9463.
(119) Hens, Z.; Moreels, I.; Martins, J. C. In situ H-1 NMR study on the trioctylphosphine oxide capping of colloidal InP nanocrystals. *ChemPhysChem* **2005**, *6*, 2578.
(120) Milner, S. T.; Lacasse, M.-D.; Graessley, W. W. Why χ is seldom zero for polymer– solvent mixtures. *Macromolecules* **2009**, *42*, 876.

(121) Alam, M. K. The effect of van der Waals and viscous forces on aerosol coagulation. *Aerosol Sci. Technol.* **1987**, *6*, 41.
(122) Sahasrabudhe, S. N.; Rodriguez-Martinez, V.; O'Meara, M.; Farkas, B. E. Density, viscosity, and surface tension of five vegetable oils at elevated temperatures: Measurement and modeling. *Int. J. Food Prop.* **2017**, *20*, 1965.
(123) Hamaker, H. C. The London—van der Waals attraction between spherical particles. *Physica* **1937**, *4*, 1058.
(124) Bergström, L. Hamaker constants of inorganic materials. *Adv. Colloid Interface Sci.* **1997**, *70*, 125.
(125) Drummond, C. J.; Chan, D. Y. van der Waals interaction, surface free energies, and contact angles: dispersive polymers and liquids. *Langmuir* **1997**, *13*, 3890.
(126) Talapin, D. V.; Shevchenko, E. V.; Murray, C. B.; Titov, A. V.; Kral, P. Dipole– dipole interactions in nanoparticle superlattices. *Nano Lett.* **2007**, *7*, 1213.
(127) Spielman, L. A. Viscous interactions in Brownian coagulation. *J. Colloid Interface Sci.* **1970**, *33*, 562.
(128) Roth, R.; Evans, R. The depletion potential in non-additive hard-sphere mixtures. *Europhys. Lett.* **2001**, *53*, 271.
(129) Lekkerkerker, H. N.; Tuinier, R. *Colloids and the depletion interaction*; Springer, 2011; Vol. 833.
(130) Asakura, S.; Oosawa, F. On interaction between two bodies immersed in a solution of macromolecules. *J. Chem. Phys.* **1954**, *22*, 1255.
(131) Aristotle *Posterior Analytics*, 350 BC.
(132) Heine, M.; Pratsinis, S. E. Brownian coagulation at high concentration. *Langmuir* **2007**, *23*, 9882.
(133) Buesser, B.; Heine, M.; Pratsinis, S. E. Coagulation of highly concentrated aerosols. *J. Aerosol Sci.* **2009**, *40*, 89.
(134) Hütter, M. Coagulation rates in concentrated colloidal suspensions studied by Brownian dynamics simulation. *Phys. Chem. Chem. Phys.* **1999**, *1*, 4429.
(135) Kusaka, Y.; Fukasawa, T.; Adachi, Y. Cluster–cluster aggregation simulation in a concentrated suspension. *J. Colloid Interface Sci.* **2011**, *363*, 34.
(136) Sciortino, F.; Belloni, A.; Tartaglia, P. Irreversible diffusion-limited cluster aggregation: The behavior of the scattered intensity. *Physical Review E* **1995**, *52*, 4068.
(137) Sciortino, F.; Tartaglia, P. Structure factor scaling during irreversible cluster-cluster aggregation. *Phys. Rev. Lett.* **1995**, *74*, 282.
(138) Bremer, L.; Bijsterbosch, B.; Walstra, P.; Van Vliet, T. Formation, properties and fractal structure of particle gels. *Adv. Colloid Interface Sci.* **1993**, *46*, 117.
(139) Richards, P. M. Diffusion and trapping at arbitrary trap size and concentration. *The Journal of chemical physics* **1986**, *85*, 3520.
(140) Richards, P. M. Diffusion to finite-size traps. *Phys. Rev. Lett.* **1986**, *56*, 1838.
(141) Richards, P. M. Diffusion to nonoverlapping or spatially correlated traps. *Physical Review B* **1987**, *35*, 248.
(142) Miller, C.; Kim, I.; Torquato, S. Trapping and flow among random arrays of oriented spheroidal inclusions. *The Journal of chemical physics* **1991**, *94*, 5592.
(143) Miller, C.; Torquato, S. Diffusion-controlled reactions among spherical traps: Effect of polydispersity in trap size. *Physical Review B* **1989**, *40*, 7101.
(144) Torquato, S. Diffusion and reaction among traps: some theoretical and simulation results. *J. Stat. Phys.* **1991**, *65*, 1173.
(145) Torquato, S. Trapping of finite-sized Brownian particles in porous media. *The Journal of chemical physics* **1991**, *95*, 2838.
(146) Lattuada, M. Predictive Model for Diffusion-Limited Aggregation Kinetics of Nanocolloids under High Concentration. *The Journal of Physical Chemistry B* **2012**, *116*, 120.
(147) Coppersmith, D.; Tetali, P.; Winkler, P. Collisions among random walks on a graph. *SIAM J. Discrete Math.* **1993**, *6*, 363.
(148) Marty, G.; Dauchot, O. Subdiffusion and Cage Effect in a Sheared Granular Material. *Phys. Rev. Lett.* **2005**, *94*, 015701.
(149) Mendez, V.; Fedotov, S.; Horsthemke, W. *Reaction-transport systems: mesoscopic foundations, fronts, and spatial instabilities*; Springer Science & Business Media, 2010.
(150) Meakin, P.; Family, F. Structure and dynamics of reaction-limited aggregation. *Phys. Rev. A* **1987**, *36*, 5498.
(151) Kim, J. S.; Yethiraj, A. Effect of macromolecular crowding on reaction rates: a computational and theoretical study. *Biophys. J.* **2009**, *96*, 1333.
(152) Pal, S.; Lan, C.; Li, Z.; Hirleman, E. D.; Ma, Y. Symmetry boundary condition in dissipative particle dynamics. *J. Comput. Phys.* **2015**, *292*, 287.
(153) Liew, K.; Seng, C.; Lee, C. Viscosities ofn-alkylamines from 15 to 80° C. *J. Solution Chem.* **1994**, *23*, 1293.
(154) Grunberg, L.; Nissan, A. H. Mixture law for viscosity. *Nature* **1949**, *164*, 799.
(155) Dymond, J.; Young, K. Transport properties of nonelectrolyte liquid mixtures—V. Viscosity coefficients for binary mixtures of benzene plus alkanes at saturation pressure from 283 to 393 K. *Int. J. Thermophys.* **1981**, *2*, 237.
(156) Flory, P. J. Intramolecular reaction between neighboring substituents of vinyl polymers. *J. Am. Chem. Soc.* **1939**, *61*, 1518.
(157) Rubinstein, M.; Colby, R. H. *Polymer Physics*; Oxford University Press, 2003.
(158) He, L.; Niemeyer, B. A Novel Correlation for Protein Diffusion Coefficients Based on Molecular Weight and Radius of Gyration. *Biotechnol. Prog.* **2003**, *19*, 544.

SYNOPSIS TOC (Word Style "SN_Synopsis_TOC"). If you are submitting your paper to a journal that requires a synopsis graphic and/or synopsis paragraph, see the Instructions for Authors on the journal's homepage for a description of what needs to be provided and for the size requirements of the artwork.

To format double-column figures, schemes, charts, and tables, use the following instructions:

Place the insertion point where you want to change the number of columns
From the **Insert** menu, choose **Break**
Under **Sections**, choose **Continuous**
Make sure the insertion point is in the new section. From the **Format** menu, choose **Columns**
In the **Number of Columns** box, type **1**
Choose the **OK** button

Authors are required to submit a graphic entry for the Table of Contents (TOC) that, in conjunction with the manuscript title, should give the reader a representative idea of one of the following: A key structure, reaction, equation, concept, or theorem, etc., that is discussed in the manuscript. Consult the journal's Instructions for Authors for TOC graphic specifications.

Insert Table of Contents artwork here
